

# UC San Diego

## UC San Diego Electronic Theses and Dissertations

### Title

Low-Temperature Liquefied Gas Electrolyte and its Application for Energy Storage

### Permalink

<https://escholarship.org/uc/item/0wv4d56j>

### Author

Yin, Yijie

### Publication Date

2020

Peer reviewed|Thesis/dissertation

UNIVERSITY OF CALIFORNIA SAN DIEGO

Low-Temperature Liquefied Gas Electrolyte and its Application for Energy  
Storage

A Thesis submitted in partial satisfaction of the requirements for the degree  
Master of Science

in

Materials Science and Engineering

by

Yijie Yin

Committee in charge:

Professor Ying Shirley Meng, Chair

Professor Zheng Chen, Co-Chair

Professor Ping Liu

2020

Copyright

Yijie Yin, 2020

All rights reserved.

The Thesis of Yijie Yin is approved, and it is acceptable in quality and form for publication on microfilm and electronically:

---

---

Co-Chair

---

Chair

University of California San Diego

2020

# DEDICATION

This thesis is dedicated to my parents,

*Hongbin Yin and Xiaoqing Sun,*

and my girlfriend, *Yizhen Lou.*

## **EPIGRAPH**

There are things you can't see unless you change your standing.

Eiichiro Oda

# TABLE OF CONTENTS

DEDICATION.....	iv
EPIGRAPH.....	v
TABLE OF CONTENTS.....	vi
LIST OF FIGURES .....	viii
LIST OF TABLES.....	x
ACKNOWLEDGMENTS .....	xi
VITA .....	xiii
ABSTRACT OF THE THESIS.....	xiv
1. Introduction .....	1
1.1. Ultra-Low Temperature Li/CF <sub>x</sub> .....	1
1.2. Capillary Condensation.....	7
2. Experimental results .....	10
2.1. Electrochemical Performance of Li/CF <sub>x</sub> .....	10
2.1.1 Electrochemical Performance of Fluoromethane-based LGE .....	14
2.1.2 Interfacial Resistance Analysis .....	15
2.2. Liquefying Gas Electrolyte by Capillary Condensation at Ambient Pressure for Extreme Low-Temperature Batteries .....	16
2.2.1. MOF's Stability with FM .....	16
2.2.2. Gas Adsorption by Capillary Effect.....	18
2.2.3. Synthesis of In-Situ MOF Growth on Graphene Oxide Film .....	21
2.2.4. Ionic conductivity measurement of MOF membrane .....	22
2.2.5. Electrochemical performance comparison in flooded liquid and gas electrolyte .....	23
2.2.6. Investigation of interfacial impedance .....	26
3. Experimental Methods .....	27
4. Conclusion.....	36

Reference.....38

## LIST OF FIGURES

<b>Figure 1:</b> Illustration of discharge process for Li/CF <sub>x</sub> battery .....	4
<b>Figure 2:</b> (a)(b) Salt solubility results of Me <sub>2</sub> O-based liquefied gas electrolytes at room temperature (RT). (c)(d) Salt solubility results of well mixed PFE and TFE-based liquefied gas. (e) The conductivity of gas/liquid electrolyte in comparison with liquid electrolyte in temperature range of -80°C to 80°C electrolytes .....	12
<b>Figure 3:</b> Discharge of Li/CF <sub>x</sub> using cosolvent A and B in LGE at -60 °C.....	14
<b>Figure 4:</b> (a) Impedance of ACN-based LGE. (b) Impedance of cosolvent B-based LGE .....	15
<b>Figure 5:</b> (a) SEM images of UiO-66. XRD patterns (b) N <sub>2</sub> sorption isotherms (c) and pore size distribution profiles (d) of UiO-66 before and after soaked in liquified FM .....	17
<b>Figure 6:</b> FT-IR (a) and Raman spectra (b) of UiO-66 before and after soaking in the FM. c, Mass change test. (d) Schematic of FM in UiO-66 at different conditions. (e) Simulated adsorption isotherms of UiO-66 confined FM. (f) Phase transition comparison between bulk FM and adsorbed FM in UiO-66 systems. ....	18
<b>Figure 7:</b> (a) Fabrication process of MPMs. N <sub>2</sub> sorption isotherm curves (b) pore size distributions (c), XRD patterns (d) of simulated UiO-66, GO@UiO-66 and MPM. (e) SEM images of GO@UiO-66. Top (f) and cross-sectional (g, h, j) SEM views of two representative MPMs (i) Nano-CT reconstruction of MPM. ....	21
<b>Figure 8:</b> (a) Ionic conductivity of pure electrolyte. (b) Ionic conductivity of LGE with the presence of MPM or Celgard-based membranes as the separator at different temperatures. Nyquist impedance of cells with MPM (c) or Celgard-based (d) membrane as the separator at -40°C and different FM pressures.....	23
<b>Figure 9:</b> Graphic illustration of (A) Flooded liquefied FM system (D) Gaseous FM system. Discharge performance of Li/CF <sub>x</sub> cell using Celgard and MPM comparison at liquefied FM system(B) and gaseous FM system(E) at -40 °C (F) The FM pressure during the discharge process at gaseous FM system. ....	25

**Figure 10:** Nyquist impedance of Li/CF<sub>x</sub> mixed with 20%wt UiO-66 using Celgard and MPM at (a) vapor pressure and (b) 70 psi at -40 °C .....26

**Figure 11:** (a) Pressure calibration of vapor pressure of FM and the mixture of FM and CO<sub>2</sub> at different temperatures. (b) Schematic description of pressure tuning process. ....32

## LIST OF TABLES

<b>Table 1:</b> Comparison of lithium-carbon monofluoride primary battery to other lithium primary batteries. The values in this table are adapted from references .....	2
<b>Table 2:</b> The physical properties of dimethyl ether, 1,1,1,2-Tetrafluoroethane (TFE), pentafluoroethane (PFE), fluoromethane, difluoromethane (DFM), propylene carbonate (PC), and tetrahydrofuran (THF).....	11

## ACKNOWLEDGMENTS

I am especially grateful to my family and my girlfriend. Without their support, this journey will not be successful.

I would like to acknowledge Prof. Ying Shirley Meng for her guidance and support as the chair of my committee. She instructs me when I know little about the electrochemical energy storage knowledge. She provides me the excellent stage and make me learn quickly and grow up.

I would like to acknowledge Prof. Zheng Chen for his strict standard and make me become strong when I face the difficulty.

I would also like to acknowledge Yangyuchen Yang without whom my research would have no doubt taken five times as long. It is their support that helped me in an immeasurable way.

I would like to thank Diyi Cheng for being great friends and participating in all the discussions that helped me improve the progress of experiments.

I would like to specially thank the liquefied gas electrolyte subgroup Daniel Davies, Matt Meyer, Katya Sablina for always being with me when I need their help.

I would also like to thank all the Laboratory for Energy Storage and Conversion (LESC) members and Chen's lab members for their unique technical skills that I could learn from and making both labs a great place to work.

I would also like to acknowledge my committee member, Prof. Ping Liu, for his support and suggestions that have strengthened this thesis.

Section 2.1 is coauthored with Yangyuchen Yang, Matthew Mayer, John Holoubek, Daniel M. Davies, Prof. Zheng Chen and Prof. Ying Shirley Meng. The thesis author is the primary author of this section.

Section 2.1.1 and 2.1.2 is coauthored with Baharak Sayahpour, Prof. Zheng Chen and Prof. Ying Shirley Meng. The thesis author is the primary author of this section.

Section 2.2 is coauthored with Guorui Cai, Dawei Xia, Amanda A. Chen, John Holoubek, Jonathan Scharf, Yangyuchen Yang, Ki Hwan Koh, Mingqian Li, Daniel M. Davies, Matthew Mayer, Tae Hee Han, Prof. Ying Shirley Meng, Prof. Tod A. Pascal and Prof. Zheng Chen. The thesis author is the primary author of this section.

## VITA

2013-2017 Bachelor of Engineering, Shanghai Jiao Tong University, Shanghai, China

2017-2020 Research Assistant, University of California San Diego, U.S.A

2017-2020 Master of Science, University of California San Diego, U.S.A

## PUBLICATIONS

Yang, Yangyuchen, Daniel M. Davies, Yijie Yin, Oleg Borodin, Jungwoo Z. Lee, Chengcheng Fang, Marco Olguin et al. "High-efficiency lithium-metal anode enabled by liquefied gas electrolytes." *Joule* 3, no. 8 (2019): 1986-2000.

Holoubek, John, Yijie Yin, Mingqian Li, Mingyu Yu, Ying Shirley Meng, Ping Liu, and Zheng Chen. "Exploiting Mechanistic Solvation Kinetics for Dual-Graphite Batteries with High Power Output at Extremely Low Temperature." *Angewandte Chemie International Edition* 58, no. 52 (2019): 18892-18897.

## FIELDS OF STUDY

Major Field: Engineering  
Studies in Materials Science and Engineering  
Professor Ying Shirley Meng  
Professor Zheng Chen

## **ABSTRACT OF THE THESIS**

Low-Temperature Liquefied Gas Electrolyte and its Application for Energy Storage

by

Yijie Yin

Materials Science and Engineering

University of California San Diego, 2020

Professor Ying Shirley Meng, Chair  
Professor Zheng Chen, Co-chair

The escalating demand for electric vehicles and importable devices has uncovered the potential of lithium-ion batteries. However, the dendrite growth concern and poor low-temperature performance of the carbonated electrolyte cannot satisfy the wide

application of the electrical devices. The advent of liquefied gas electrolytes has proven to be one of the most promising alternatives to extend the temperature operation range of commercial rechargeable batteries to extremely cold conditions and eliminate the dendrite growth for the long-term cycling. In this work, the mechanism of the liquefied gas electrolytes, especially its low-temperature mechanism has been explored and the solution to lower its inside pressure is also investigated. In this first part, a new liquefied fluoromethane electrolyte with the additive is shown to be competitive for low-temperature primary Li/CF<sub>x</sub> system compared with SOA. In the second part, the liquefied gas electrolyte is counteracted by its high vapor pressure, prohibiting its practical application. Herein, we construct a mimetic “brick-and-mortar” microstructure of MOF-polymer membrane, which enables the capillary condensation effects to effectively liquefy hydrofluorocarbon gas molecules in lithium cells under reduced pressure. This strategy opens a pathway to liquefying hydrofluorocarbon molecules under ambient pressure for the fabrication of lithium cells using gaseous solvents like the way in conventional liquid cell fabrications.

# 1. Introduction

## 1.1. Ultra-Low Temperature Li/CF<sub>x</sub>

The advancement of high performance, safe, and long shelf-life primary battery systems are vital for NASA's lunar and Mars' surface exploration initiatives requiring human and robotic operation in harsh environments (i.e. ultra-low temperature, radiation, complex terrain). However, contemporary battery technologies paired with complex thermal management systems, which provide less than 200 Wh/kg at temperatures between -40°C and -80°C, cannot satisfy these requirements. Given the added complexity, weight, and cost of external heating or internal self-heating systems, advancing the battery chemistry to operate at these extreme temperatures is a more efficient approach. Here, we propose to develop a reliable high-performance primary lithium metal battery system using fluorinated graphite (CF<sub>x</sub>) as the active material of the cathode. The main objective of this work is to enable a cell-level energy density of >400 Wh/kg at C/720 in the temperature range of -40°C to -120°C without any reliance on secondary heating solutions. NASA's increasing interest in the surface exploration of the Moon and Mars requires a more sustainable power supply for sustaining the long-period (few weeks) operations at harsh space environments. Given the ultra-low average surface temperatures, high radiation, and moderate long-distance from the Sun, primary batteries become one of the few reliable power source candidates<sup>1-2</sup>. Amongst the well-known primary batteries (Table 1), Li/CF<sub>x</sub> presents the highest theoretical specific capacity and energy density, while e.g. Li/I<sub>2</sub>, Li/MnO<sub>2</sub>, Li/Ag<sub>2</sub>CrO<sub>4</sub>, and Li/CuS suffer from reduced theoretical energy density<sup>3-5</sup>. For example, the continuous growth of LiI interface will significantly decrease its low-temperature performance. Moreover, Li/CuS suffers

from its low nominal voltage (1.2V) and Li/MnO<sub>2</sub> battery suffers from a cathode swelling(gassing) at rest stage. Although Li/SOCl<sub>2</sub> has high energy density (1470 Wh/kg) and nominal voltage (3.6 V), its remaining safety concerns make it unsuitable for space applications. On the contrary, CF<sub>x</sub> is a light weight, safe, and highly stable system which displays a low self-discharge rate with <0.5 % per year at room temperature<sup>2</sup>. However, low electrical conductivity and strong C-F bonds results in slow cell reaction kinetics. This further leads to poor low-temperature performance.

**Table 1:** Comparison of lithium-carbon monofluoride primary battery to other lithium primary batteries. The values in this table are adapted from references

<b>Cell Chemistry</b>	<b>Theoretical Capacity (mAh/g)</b>	<b>Theoretical Energy Density (Wh/kg)</b>
Li/CF <sub>x</sub>	865	2180
Li/SOCl <sub>2</sub>	450	1470
Li/CuS	560	1050
Li/MnO <sub>2</sub>	310	1005
Li/I <sub>2</sub>	211	591
Li/Ag <sub>2</sub> CrO <sub>4</sub>	160	515

When the battery is exposed to sub-zero temperatures, several aspects are influencing its low-temperature performance (Figure 1): (i) Li<sup>+</sup> diffusion through the solid electrolyte interface (SEI) and

carhode electrolyte interface (CEI) layers; (ii) Li<sup>+</sup> solvation and de-solvation processes; (iii) Li<sup>+</sup> diffusion through bulk electrolytes; (iv) Solid-state diffusion in CF<sub>x</sub> layers; (v) Redox reactions. Therefore, current research efforts to improve low-temperature performance encompasses electrolyte optimizations, electrode modifications, and interfacial engineering<sup>6-10</sup>.

#### (1) Electrolyte optimization

The widely used carbonate-based electrolytes in the lithium-ion field suffers from poor low-temperature performance due to its relatively high freezing point and high viscosity, which hinders Li<sup>+</sup> transport at reduced temperatures. To improve the electrolyte ionic conductivity without sacrificing chemical stability with lithium metal, NASA's Jet Propulsion Laboratory (JPL) firstly reported electrolyte formulations that consist of 1 M LiBF<sub>4</sub> (lithium tetrafluoroborate) paired with 4:1 dimethoxyethane (DME): propylene carbonate (PC), which could deliver more than 600 mAh/g capacity at C/40 rate under -40°C. This work also demonstrated the pre-discharge step which discharges around 3% of total estimated capacity using C/33 rate at room temperature<sup>11</sup>. This step significantly improved the cell capacity from less than 100 mAh/g to more than 600 mAh/g and the discharge voltage from around 1.9 V to 2.2 V at -40 °C. The optimized work done by the same group after lowering the salt concentration and adding the tris(2,2,2-trifluoroethyl) borate (TTFEB), enhanced the specific capacity to around 300 mAh/g at C/5 rate under -60°C. Additionally, another study showed that using acetonitrile (ACN) to pursue the concept of electrolytes with lower viscosity compared with DME. In order to overcome the instability of ACN towards lithium metal, they proposed to mix ACN with  $\gamma$ -butyrolactone (BL) to improve the stability of the lithium metal anode by the formation of a dense protective passivation film on the lithium metal surface<sup>12</sup>. They showed that the ACN system outperformed the DME system at both power capability and low-temperature

discharge performance. This was due to its overwhelmingly higher ionic conductivity which facilitated bulk electrolyte transport at low temperatures. Overall, the SOA ether-based and nitrile-based electrolytes are still facing severe overpotential and capacity loss which have more than 0.7 V voltage decay and 50% capacity loss at  $-60^{\circ}\text{C}$  when discharged at C/10 or even smaller rates. Additionally, there is no available electrolyte in literature addressing the theoretical freezing point down to  $-120^{\circ}\text{C}$ . Therefore, a new strategy for electrolyte design is required for high energy density of Li/CF<sub>x</sub> at low temperatures below  $-60^{\circ}\text{C}$ .

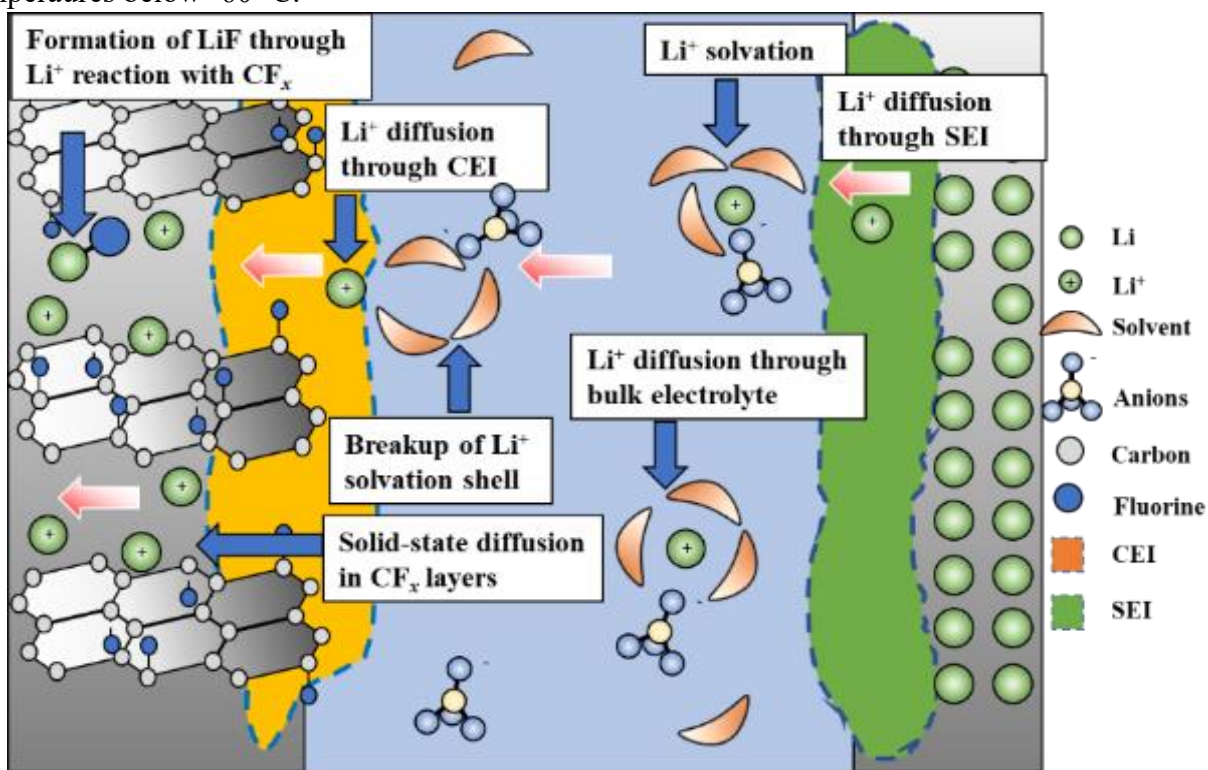


**Figure 1:** Illustration of discharge process for Li/CF<sub>x</sub> battery

## (2) Cathode Modifications

A key factor limiting the high-rate performance of Li-CFx systems at low temperatures is the low intrinsic conductivity of CF<sub>x</sub> cathode due to the nature of covalent C-F bonds. To address this issue for low-temperature cathodes, there have been a few studies mainly focused on the following strategies: (i) using a thinner electrode to decrease the cell resistance, (ii) utilizing a sub-fluorinated

carbon which has been attributed to better electronic conductivity, and (iii) employing CF<sub>x</sub>-MnO<sub>2</sub> hybrid structure as a co-catalytic cathode to improve the reaction kinetics.

Previously, utilization of sub-fluorinated graphitic carbon (CF<sub>0.65</sub>) with a better electronic conductivity along with a room-temperature pre-discharge step was reported to deliver a higher energy density compared to fluorinated graphite (CF<sub>1.08</sub>). Using the same PC:DME (1:4) with 1M LiBF<sub>4</sub> as the electrolyte, it has been shown that commercial CF<sub>1.08</sub> with excess carbon conductive agent (30%) delivered about 200 mAh/g discharged capacity (C/40) at -40°C while this discharged capacity increased to about 600 mAh/g with the same condition using CF<sub>0.65</sub>. Later, another group investigated four different commercial CF<sub>x</sub> (0.8<x<1.2) along with two different electrolytes in the temperature range of -51°C to 72°C<sup>13-16</sup>. These studies confirmed the importance of structural modification and their effect on ionic and electronic conductivity for improved electrochemical performance of CF<sub>x</sub> cathodes. Despite the limited studies to overcome the electronic conductivity barrier of the CF<sub>x</sub> cathode, such as using the thinner electrodes or sub-fluorinated carbon, there are still many outstanding questions and challenges for low-temperature performance of this system. (i) it is not well-understood what is the effect of the size, thickness, and morphology of CF<sub>x</sub> particles on the performance of CF<sub>x</sub> cathodes at low temperatures. (ii) a systematic study on ionic and electronic conductivity of CF<sub>x</sub> cathode materials at different temperatures, e.g. room temperature compared to low temperature (-40°C or lower). Addressing such questions can lead to a better understanding of the current limitations of low-temperature CF<sub>x</sub> cathodes and improving their performance.

### (3) Understanding and Improving Electrode/Electrolyte Interface

Besides the bulk electrolyte and electrode transport kinetics, the charge transfer resistance across the cathode/electrolyte and anode/electrolyte interfaces significantly affects the overpotential

during discharge at low-temperature. Addressing the key factors to eliminate the overpotential increase is of great importance; (i) fast Li<sup>+</sup> transport through the electrode/electrolyte interface to facilitate the Li<sup>+</sup> solvation and de-solvation processes, and (ii) continuous chemical reactions to break the C-F bonds and reform uniform Li-F bonds. To understand the interfaces for Li/CF<sub>x</sub> primary batteries, a few studies have been done focusing on electrochemical techniques, such as electrochemical impedance spectroscopy (EIS) and Tafel measurements. The elemental and morphological characterizations of interface layers are currently missing. However, understanding of temperature effects upon SEI/CEI and strategies for enabling low impedance film for Li/CF<sub>x</sub> battery can be referred from some lithium metal-related work. For example, one previous study indicated that the temperature factor exerts a non-negligible influence on the morphology and chemistry of the films formed at the lithium metal anode, where smaller particle size had been observed at -40°C compared to room temperature. Another study designed a low impedance interface film using a lithium difluorobis(oxalato) phosphate (LiDFBOP) additive at the anode and cathode side to improve the low-temperature performance. Besides that, another study has shown that by adding a small amount of fluoroethylene carbonate (FEC) into the PC+DME+tetrahydrofuran (THF) ternary blend using lithium perchlorate (LiClO<sub>4</sub>) salt, the impedance from the lithium metal side Li/CF<sub>x</sub>-MnO<sub>2</sub> dropped significantly, particularly at -40°C. Overall, some fundamental questions have not been addressed for Li/CF<sub>x</sub>. (i) The chemical composition and morphology of CEI formed at room and low temperatures. (ii) The chemical composition and morphology of SEI preventing lithium metal from continuously reacting with electrolytes to achieve a long storage life. (iii). The effect of the electrolyte upon SEI and CEI's stability that facilitates long shelf-life.

## 1.2. Capillary Condensation

Confining molecules in nanoscale can lead to dramatic changes in their physical and chemical properties, which opens possibilities for new applications. There is a growing interest in liquefied gas electrolytes for batteries operating at low temperatures due to their low freezing point. However, their high vapor pressure poses potential safety concerns for practical usages. Herein, we report capillary condensation of gas electrolyte by strong confinement in sub-nanometer pores of metal-organic framework (MOFs). By designing MOF-polymer membranes (MPMs) that present dense and continuous micropore (~0.8 nm) networks, we show significant uptake of hydrofluorocarbon molecules in MOF pores at pressure lower than the bulk counterpart. This unique property enables MPM-based electrolytes to deliver a significantly higher capacity than those with commercial separator membranes (~ 500 mAh g<sup>-1</sup> vs. < 0.03 mAh g<sup>-1</sup>) at -40 °C under reduced pressure of the electrolyte.

Batteries that can sustain extremely cold temperatures (< -30 °C) are essential for extending the operation capability of existing energy storage systems as well as enabling human presence to the deep space and deep ocean worlds. The state-of-the-art lithium-ion batteries (LIBs) are mostly restricted to perform in mild conditions due to the drastically decreased ionic conductivity and increased charge transfer impedance of electrode/electrolyte interfaces at ultra-low temperatures. Although many approaches (e.g., externally/internally heating, cell insulating, and introducing co-solvents or additives) have been developed to overcome the above issues, no current technology extends the operating temperature range of batteries without sacrificing the long-term stability and energy density<sup>17-23</sup>.

Unlike conventional liquid/solid electrolyte chemistries, liquefied hydrofluorocarbon gas molecules like fluoromethane (FM) shows an extremely low melting point (-142 °C) and low viscosity (0.085 mPa·s), which enable electrolytes with high ionic conductivity and superior lithium metal compatibility down to temperatures as low as -60 °C. To retain the electrolyte in the liquid state, the gas molecules need to be maintained at its vapor pressure ( $P_v$ ). However, the saturated vapor pressure for these gas molecules is quite high ( $P_{sat}$ , FM = 495 psi or 33 atm at 20 °C), which would render safety concerns in practical devices.

To address the above-mentioned electrolyte limitation, it is conceivable to exploit capillary condensation, a phenomenon whereby gas molecules in small confined pores condense into a liquid at an equilibrium pressure  $P_v$  is lower than the bulk vapor pressure  $P_{sat}$ . The relationship between the  $P_v$  and the  $P_{sat}$  follows the Kelvin equation:

$$\ln \frac{P_v}{P_{sat}} = \frac{2\gamma V_L}{rRT}$$

where  $\gamma$  is the liquid/vapor surface tension,  $V_L$  the molar volume of the liquid adsorbate,  $r$  the mean radius of curvature of the liquid/gas interface (proportional to pore radius),  $R$  the universal gas constant, and  $T$  the absolute isothermal temperature. Generally, smaller  $r$  values enable a lower  $P_v$  to condense gas molecules at a given temperature. For example, both simulation and experimental results show that the actual pressure required to condense nitrogen molecules in porous carbon (slit-shaped pores) reduces by > 10 times as the pore diameter decreases from 7 nm to 1 nm. Similar trends have also been observed for methane absorption and condensation in nanopores. Hydrofluorocarbons share some similar physicochemical characteristics with methane (e.g., high vapor pressure, low melting point), yet capillary condensation of hydrofluorocarbon has not been explored, nor has there

been a study reporting the design of a stable nanoporous host to condense gas molecules at reduced pressures for electrochemical applications.

Metal-organic frameworks (MOFs), a class of porous crystalline solids assembled by organic linkers and metal ions/clusters, could be ideal candidates to capture FM molecules via capillary condensation to lower the inner pressure of batteries employing liquefied gas electrolytes (LGE). Various MOFs have been successfully applied for the storage or separation of carbon dioxide, methane, and alkene molecules<sup>24-27</sup>. Composites formed from MOF particles and polymer binders have been employed as separator membranes of LIBs for an increased  $\text{Li}^+$  transference number based on the size-selective effect of MOF pores. However, such MOF-based membranes are not suitable for desired ion migration in LGE under reduced pressure, due to the presence of numerous gaps between the binders and MOF particles which inevitably degrade the continuous liquefied gas flux required for  $\text{Li}^+$  migration throughout the entire membrane.

Pure MOF membranes have been reported for gas adsorption/separation and solid electrolyte, however their poor mechanical properties and large thickness (typically  $>100 \mu\text{m}$ ) inhibit their applications in batteries<sup>28-30</sup>. MOF particles have therefore been combined with commercial Celgard membranes or other porous substrates to improve the mechanical properties of the resulted MOF-based membranes. However, additional substrates increase the separator thickness and hinder the cathode – anode ion pathway at reduced pressures. Therefore, it is prerequisite to develop a mechanically robust, self-supporting MOF-based porous membrane with small thickness and minimal macro-voids for continuous ionic transport in LGE, especially at reduced pressure.

In first part of this thesis, we will demonstrate the potential of Li/CFx in the liquefied gas electrolyte at reduced temperature and investigate the preliminary interfacial impedance which limits

the low-temperature performance. The second part of the report will focus on low pressure liquefied gas electrolyte enabled by the MOF-based membrane and the future experimental plans.

## **2. Experimental results**

### **2.1. Electrochemical Performance of Li/CF<sub>x</sub>**

To address the low temperature limitations, a paradigm-shift design tailored for extremely low-temperature primary Li-CF<sub>x</sub> cells that are based on liquified-gas electrolytes. Such a unique electrolyte will integrate the gaseous molecules that offer the lowest possible freezing point among existing electrolytes and co-solvent additives to endow additional functionality for improved stability, safety, and kinetic properties compared with previously reported systems. Specifically, this Li-CF<sub>x</sub> cell system will form an electrolyte (gas/liquid (GL) mixture electrolyte) with a freezing point lower than -120°C, a wide electrochemical window (0-4.3V vs. Li/Li<sup>+</sup>), and low flammability, with ionic conductivity more than 1 mS/cm at -60°C or lower temperature.

We will leverage our knowledge of established liquefied gas electrolyte and novel low-temperature liquid-based electrolytes for lithium metal Li/NMC batteries based on team's previous work. Unlike earlier work on using fluoromethane predominated (occupied more than 90 % volume ratio) liquefied gas electrolyte, we will formulate a mixture of liquefied gaseous solvents and liquid solvents which has a balanced volume ratio. This will combine the merit of gaseous solvent which has a melting point down to -120 oC, viscosity less than 0.1 mPa\*S, and moderate dielectric constant, as well as the liquid electrolyte such as PC or FEC to improve the stability with lithium metal and fasten the lithium-ion solvation process at the lithium metal side.

**Table 2:** The physical properties of dimethyl ether, 1,1,1,2-Tetrafluoroethane (TFE), pentafluoroethane (PFE), fluoromethane, difluoromethane (DFM), propylene carbonate (PC), and tetrahydrofuran (THF).

Solvent	Melting Point (°C)	Boiling Point(°C)	Critical Point(°C)	Flash Point	Vapor Pressure (psi)	Dipole	Dielectric Constant	Viscosity (mPa·s)
Dimethyl Ether	-141	-24	127	-41	75	1.3	5.02	-
1,1,1,2-Tetrafluoroethane	-103	-26.3	101	250	82	2.06	9.7	0.207
Pentafluoroethane	-103	-48.5	66	None	175	1.56	4.5	0.15
Fluoromethane	-142	-78	44	Flammable	479	1.85	9.7	0.085
Difluoromethane	-136	-52	78	Flammable	247	1.98	14.2	0.12
Propylene Carbonate	-48.8	242	377	135	0.003	4.9	64.9	2.5
Tetrahydrofuran	-108	66	268	-17.2	2.77	1.75	7.52	0.456

We have identified dimethyl ether (Me<sub>2</sub>O) as a new class of ether-based liquefied gas solvents which has a freezing point down to -140 °C, low vapor pressure at around 75 psi at ambient temperature, and a moderate dielectric constant at around 5.02 (Table 2)<sup>31-34</sup>.

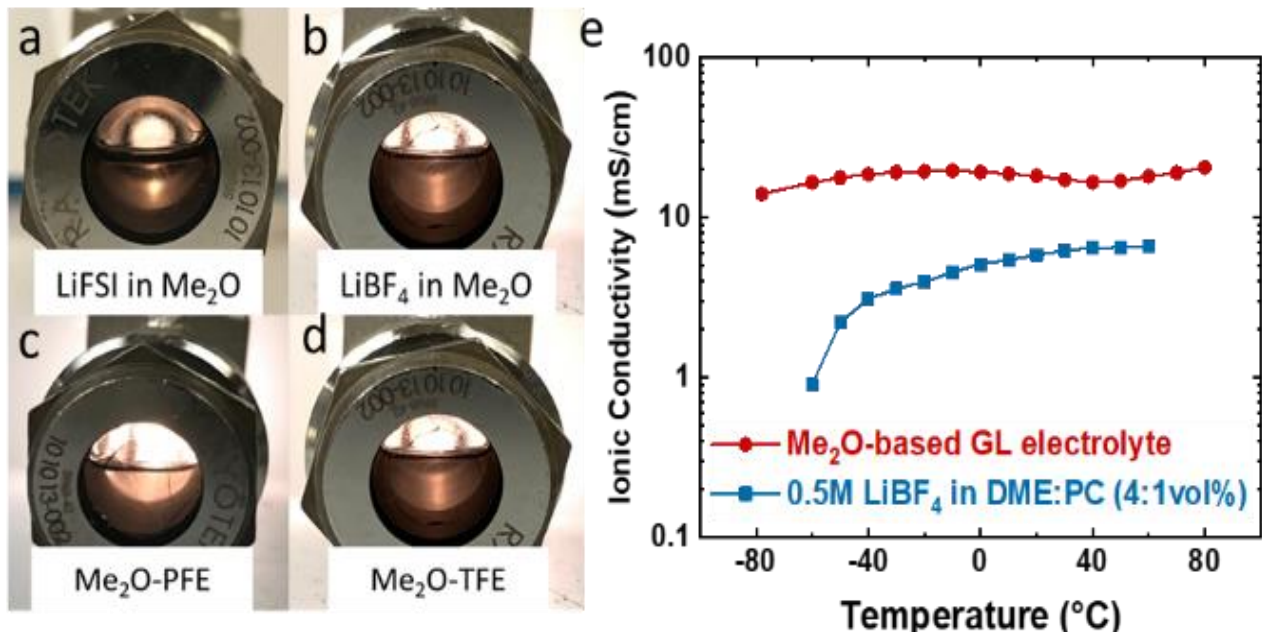


**Figure 2:** (a)(b) Salt solubility results of Me<sub>2</sub>O-based liquefied gas electrolytes at room temperature (RT). (c)(d) Salt solubility results of well mixed PFE and TFE-based liquefied gas. (e) The conductivity of gas/liquid electrolyte in comparison with liquid electrolyte in temperature range of -80°C to 80°C electrolytes

Unlike previous generally used fluoromethane-based gaseous solvent which has less than 0.1 M salt solubility, while dimethyl ether has more than 1 M salt concentration solubility for different kinds of salts. Our preliminary results showed that Me<sub>2</sub>O-based liquefied gas electrolytes can dissolve both LiFSI and LiBF<sub>4</sub> salts (Figure 2(a)-(b)). Moreover, from our preliminary ionic conductivity test, dimethyl ether-based GL mixture electrolyte exhibited more than 12 mS/cm ionic conductivity at -78°C (Figure 2(e)), which is more than one-order of magnitude higher than the SOA electrolyte at that temperature. The conductivity trend for this type of electrolyte when compared to 0.5 M LiBF<sub>4</sub> in 4:1vol% DME:PC liquid electrolytes show us higher resilience when the temperature drops below -78°C. This implied that our electrolyte is suitable for ultra-low temperature ranges as it can remain liquid even as low as -120°C. Additionally, functional co-solvents will be explored to (i) passivate the

lithium metal surface, (ii) improve the solvation process of  $\text{Li}^+$  coordinated with solvents and salts, and (iii) enhance the safety. For instance, using carbonate-based solvents such as PC or FEC, will improve the chemical stability with lithium metal. Given the importance of safety, we also propose to include some fire-retardant agents as electrolyte additives to improve non-flammability. Table 2 showed several gas candidates such as 1,1,1,2-Tetrafluoroethane (TFE) and Pentafluoroethane (PFE) which are generally used as fire-extinguisher agents which could potentially enable low pressure, fire-retardant electrolytes. Our preliminary study has proven their good solubility of this type of co-solvents with various lithium salts, cosolvents (Figure 2(c)(d)). Due to their inertness of coordinating with  $\text{Li}^+$ , it will also be beneficial for formulating a locally-high concentrated electrolyte system. Based on our preliminary results, this strategy of novel electrolyte design seems promising to push forward the low temperature performance.

Section 2.1 is coauthored with Yangyuchen Yang, Matthew Mayer, John Holoubek, Daniel M. Davies, Prof. Zheng Chen and Prof. Ying Shirley Meng. The thesis author is the primary author of this section.

### 2.1.1 Electrochemical Performance of Fluoromethane-based LGE

Firstly, we explored fluoromethane-based liquefied gas electrolyte system. From the earlier work, we demonstrate the potential of low-temperature Li/SS plating and stripping at  $-60\text{ }^{\circ}\text{C}$ , which maintains an average high coulombic efficiency of 98.7%. Due to its high ionic conductivity at such low temperature, we choose the  $\text{CF}_x$ , which is known to have the highest theoretical capacity as our candidate cathode for low temperature primary battery. Figure 3 shows discharge data from  $\text{CF}_x$  using C/20 current with AN(acetonitrile)-based LGE (Cosolvent A) and THF-based LGE (Cosolvent B) and 0.5 M  $\text{LiBF}_4$  in 4:1 DME:PC as the comparison electrolyte both at room temperature and  $-60\text{ }^{\circ}\text{C}$ . Among all of them, the AN cosolvent in the LGE show the best performance both at room temperature and at  $-60\text{ }^{\circ}\text{C}$ .

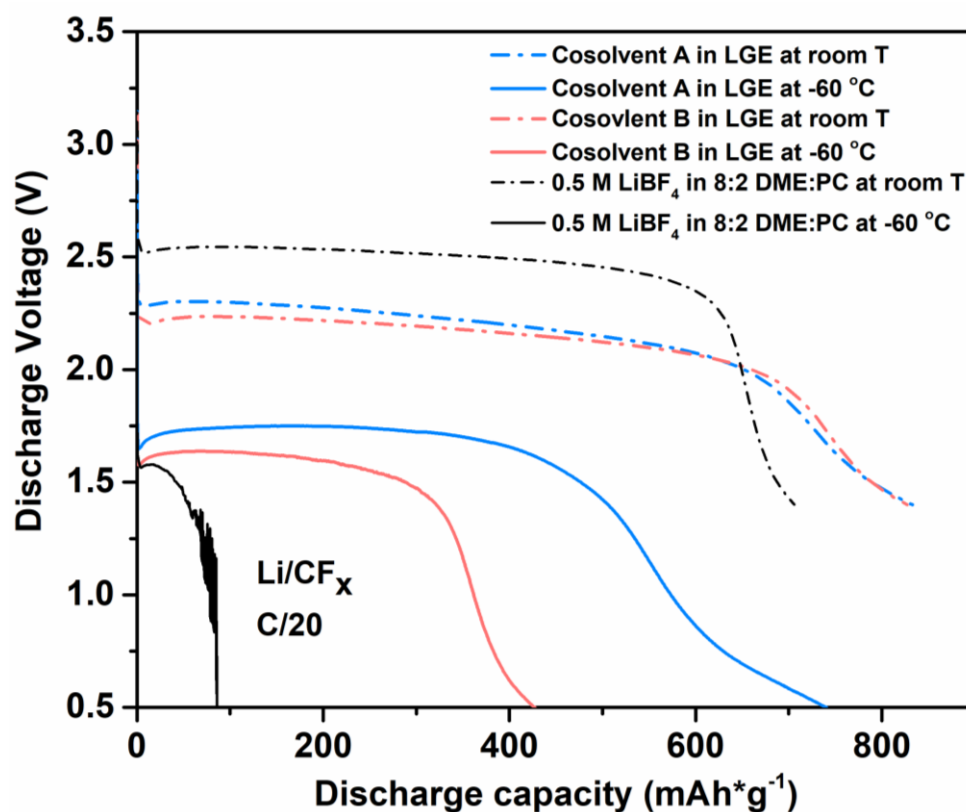


Figure 3: Discharge of  $\text{Li}/\text{CF}_x$  using cosolvent A and B in LGE at  $-60\text{ }^{\circ}\text{C}$

Due to the low viscosity and high ionic conductivity of LGE electrolyte, both cosolvent combined with LGE shows much better capacity retention at -60 °C. However, the comparative electrolyte only remains 12% capacity compared with room temperature capacity. This excellent performance successfully indicates the LGE is capable of being used as the low temperature Li/CFx primary battery which provides more than 75% room temperature capacity at such low temperature. To fully understand the interfacial resistance, the electrical impedance spectroscopy (EIS) has been collected.

### 2.1.2 Interfacial Resistance Analysis

Figure 4(a,b) shows the cosolvent A has lower both electrolyte/electrode resistance and charge-transfer resistance, which is mainly influenced by the Li<sup>+</sup> de-solvated from the solvation shell. During the discharging, there are two balanced processes that happen at the same time. One is the formation of the electrically conductive graphite and the other is the growth of the GIC (Graphite intercalation compound) layer which is surrounded by the insoluble LiF, functioning as the insulator. So the lower charge transfer impedance explains the better solvation structure of nitrile-based cosolvent in LGE.

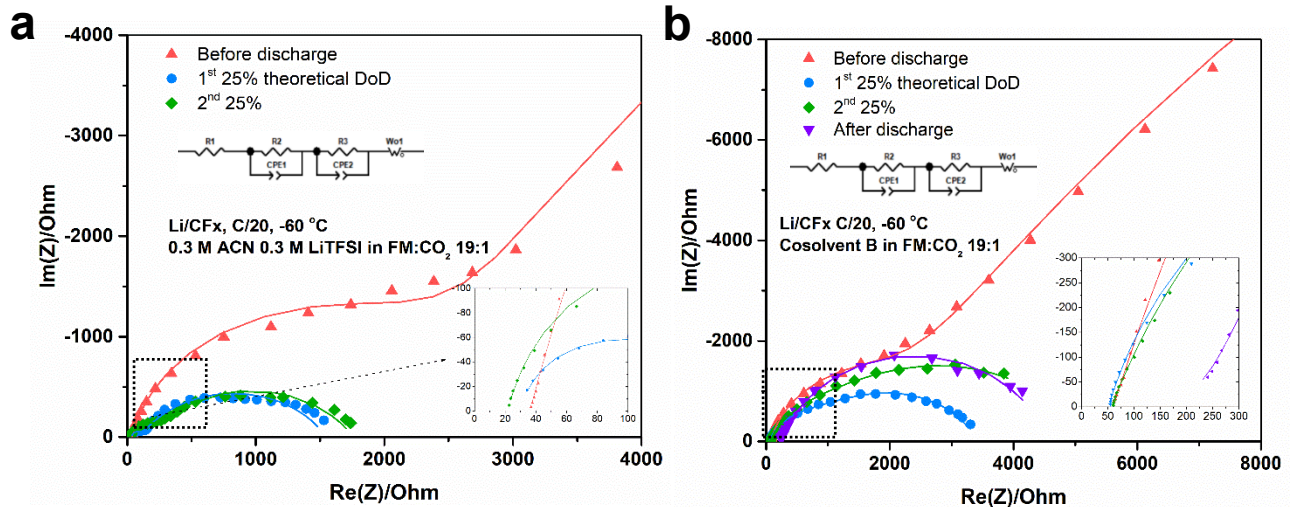


Figure 4: (a) Impedance of ACN-based LGE. (b) Impedance of cosolvent B-based LGE

Section 2.1.1 and 2.1.2 is coauthored with Baharak Sayahpour, Prof. Zheng Chen and Prof. Ying Shirley Meng. The thesis author is the primary author of this section.

## **2.2. Liquefying Gas Electrolyte by Capillary Condensation at Ambient Pressure**

### *2.2.1. MOF's Stability with FM*

In order to identify a suitable MOF as the building blocks of MPM, a series of MOFs (HKUST, MOF-808, UiO-67, and UiO-66) with large pore volumes were tested and compared in terms of chemical/structural stability with FM.<sup>35-38</sup> To determine compatibility, as-synthesized MOF powders were subject to various characterizations before and after soaking in liquid FM. From N<sub>2</sub> sorption isotherms and the associated X-ray diffraction (XRD) patterns, it was found that all the selected MOFs maintained their crystallinity and highly microstructure features after exposure to FM, even at high pressure (~500 psi, room temperature). To further probe their potential as battery separators, a common solution-casting approach of directly mixing MOF powders and poly(vinylidene fluoride-co-hexafluoropropylene) (PVDF-HFP) binder solutions was used to produce MOF-based mixed matrix membranes (MMMs). Note that from the fabrication point of view, such as method provides a simple and consistent way to screen different MOFs. The ionic conductivities in liquefied FM-based electrolytes were tested by using each corresponding MMM as a separator membrane. It was revealed that among various MOFs, UiO-66 and UiO-67 based MMMs provided the highest ion conductivity. Of note, at -60 °C the UiO-66 MMM exhibited an ionic conductivity of 0.67 mS/cm while UiO-67 exhibited 0.75 mS/cm, higher than that of Celgard 2400 (0.36 mS/cm). When the temperature was increased to 20 °C, UiO-66 maintained a conductivity of 0.54 mS/cm, much higher than that of Celgard (0.16 mS/cm) and UiO-67 (0.35 mS/cm).

Based on the confirmed chemical stability in the presence of liquid FM and high ionic conductivity with LGE, UiO-66 was selected as the host structure for subsequent development of MPM. and the value of  $1424 \text{ m}^2 \cdot \text{g}^{-1}$  in soaked UiO-66 has been obtained for immersing into the FM, which considered as the dehydration and activation process.

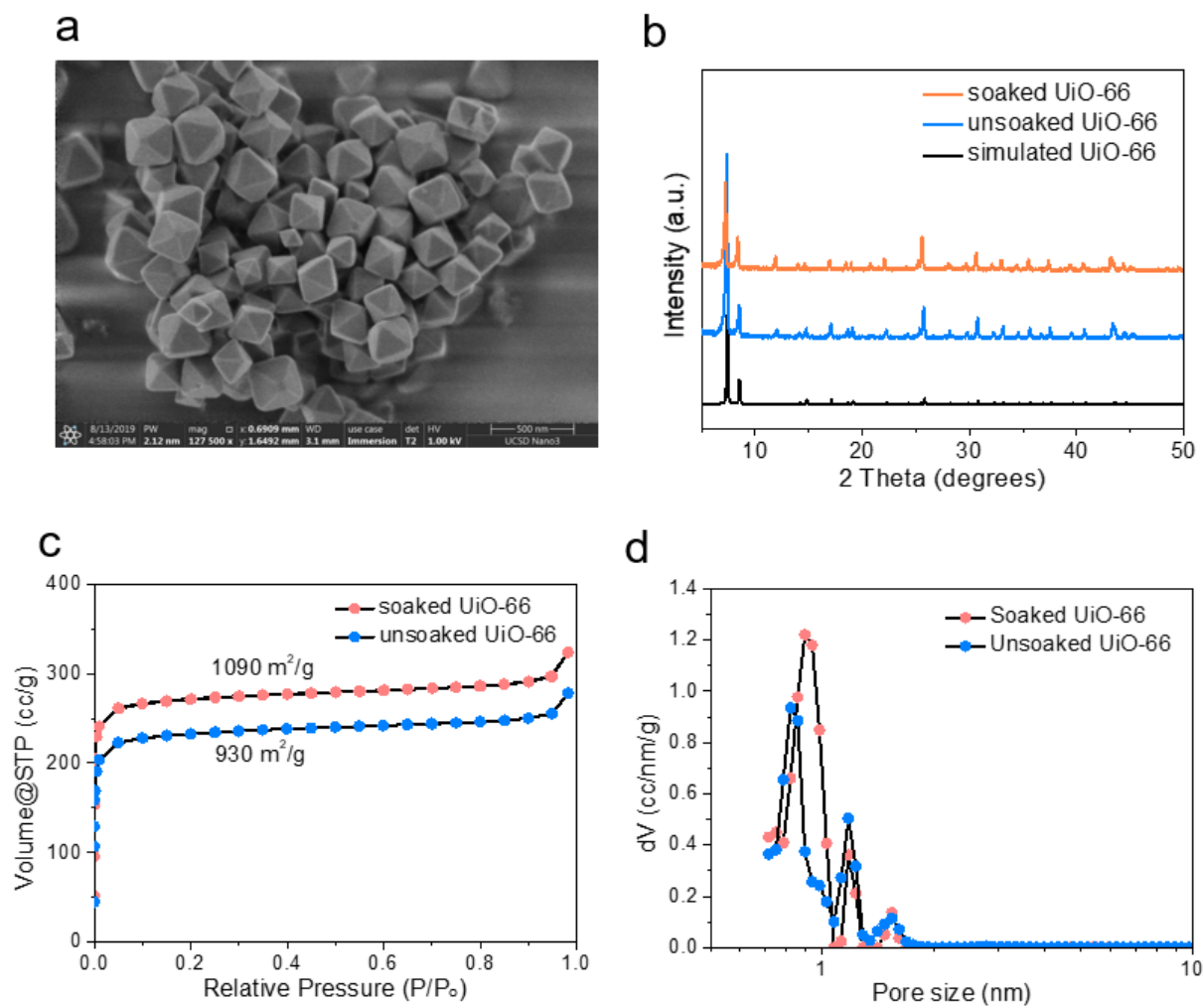


**Figure 5:** (a) SEM images of UiO-66. XRD patterns (b) N<sub>2</sub> sorption isotherms (c) and pore size distribution profiles (d) of UiO-66 before and after soaked in liquified FM

## 2.2.2. Gas Adsorption by Capillary Effect

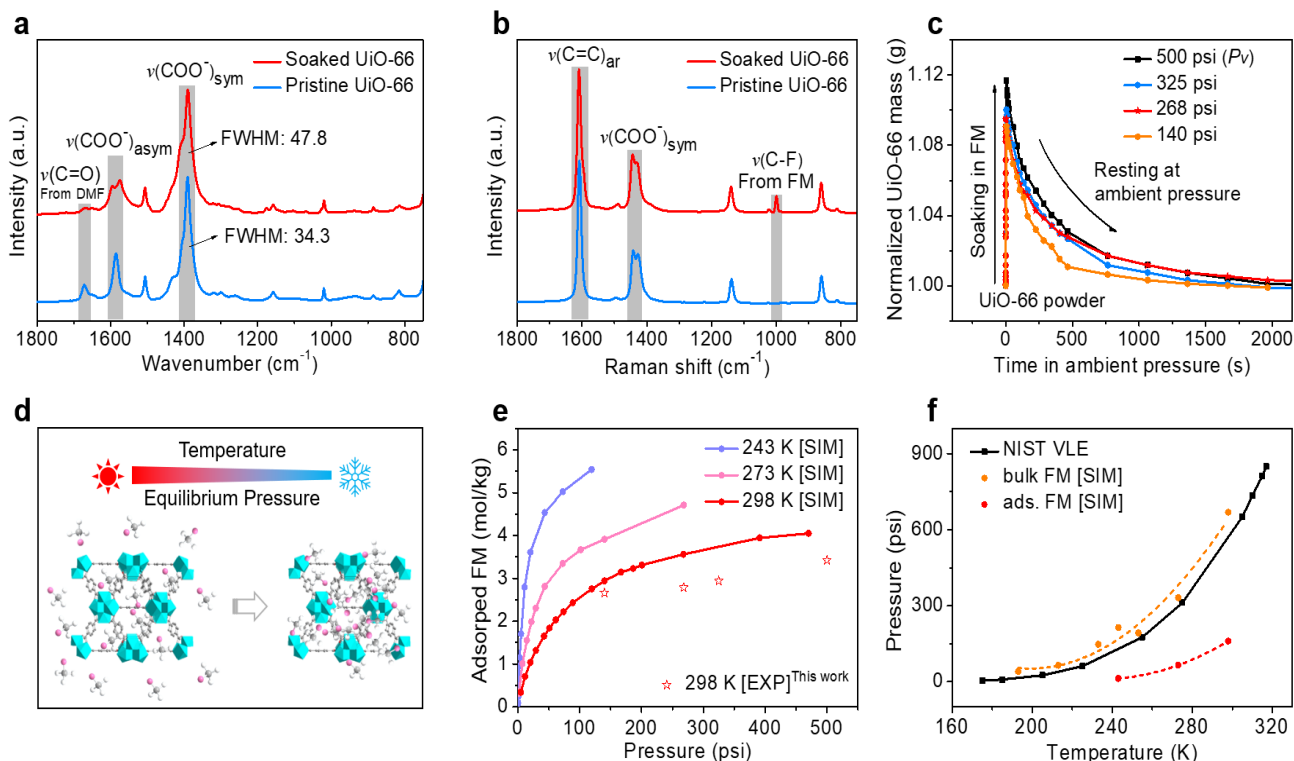


**Figure 6:** FT-IR (a) and Raman spectra (b) of UiO-66 before and after soaking in the FM. c, Mass change test. (d) Schematic of FM in UiO-66 at different conditions. (e) Simulated adsorption isotherms of UiO-66 confined FM. (f) Phase transition comparison between bulk FM and adsorbed FM in UiO-66 systems.

The  $\text{N}_2$  sorption isotherms of UiO-66 after soaking in liquid FM exhibited an increased surface area and pore volume, indicating an activation process of FM due to the strong interaction between FM and the open metal sites in UiO-66, similar to the supercritical  $\text{CO}_2$  activation of MOF pores.<sup>27</sup> From the Fourier transform-infrared (FT-IR) spectrum (Fig. 6a), it was observed that the symmetric  $\text{COO}^-$  ( $\nu_{\text{sy}}\text{COO}^-$ ) stretching mode at around  $1392 \text{ cm}^{-1}$  broadened after FM soaking (full width at half maximum (FWHM): 47.8 vs. 34.3), which indicated strong chemical interactions between the UiO-66 and FM.<sup>42,43</sup> This was further supported by the Raman spectra, in which the peak of the symmetric stretching mode at around 1444 and  $1428 \text{ cm}^{-1}$  exhibited a change of shape (Fig. 6b).<sup>42</sup> In addition, the signal of DMF molecules presented in the MPM gradually decreased with the increase of soaking processes, indicative of the

replacement of DMF with FM (Fig. 6b). It was also observed that the Raman spectra of FM soaked samples exhibited a characteristic peak at  $1000\text{ cm}^{-1}$ , attributed to the C-F vibration of the FM (Fig. 6b), indicating FM was still present in the UiO-66 pores even at ambient pressure. All the above results revealed that UiO-66 was able to firmly confine FM molecules beneath their vapor pressure.

In order to quantify the FM absorption capability of UiO-66, a direct measurement of FM uptake in the UiO-66 powders was performed after immersing the UiO-66 powders into FM with various pressures for three days. After purging out the bulk FM from the customized high-pressure cell, the total mass of the soaked UiO-66 powders was *in-situ* measured in an Ar-filled glove box under ambient pressure. The mass difference of UiO-66 before and after the soaking process was considered as the mass change caused by the absorbed FM. As shown in Fig. 6c, the mass of the UiO-66 powders increased by  $\sim 12\%$  after soaking at  $\sim 500$  psi, demonstrating the ability of UiO-66 to store of a large volume of liquefied FM molecules (corresponding to molar ratio of FM:UiO-66 at 5.7:1 for the absorbed sample).

Further insights into the microscopic interactions between FM and UiO-66 was acquired from computer simulations (Fig. 6d). Both quantum mechanical calculations and molecular dynamic simulations were applied, as detailed in Computational details of Methods. All simulated adsorption isotherms of FM in UiO-66 at variable temperatures exhibited a classical type I isotherm of micropore adsorption (Fig. 6e,f), in which UiO-66 achieved a 10% mass uptake of FM at 140 psi and  $25\text{ }^\circ\text{C}$ , in good agreement with our experiments (9% mass uptake at 140 psi,  $25\text{ }^\circ\text{C}$ ). In addition, we found the density of FM in UiO-66 was significantly increased compared to the bulk fluid. It was shown that the FM density increased from  $0.3\text{ mol/L}$  (bulk FM) to  $3\text{ mol/L}$  (ads. FM in UiO-66) at 100 psi,  $25\text{ }^\circ\text{C}$ . We quantified the capillary condensation of FM in UiO-66 by considering the thermodynamics of the equilibrated system using the Two-Phase Thermodynamics Method.<sup>44,45</sup> In particular, we determined the phase change behavior of FM by a novel approach, considering the fraction of the FM modes that were diffusive, hereby

denoted the “fluidicity (f)-factor”. This approach is necessary because while the phase boundaries of a bulk homogenous fluid are given by solutions to the Clausius-Clapeyron equation,<sup>46</sup> computational schemes typically rely on locating discontinuities in the relevant thermodynamic functions, such as the molar enthalpy.<sup>47</sup> In the particular case of FM in UiO-66, we found that the molar enthalpy function showed significant uncertainty, especially at low pressures, which obscured unambiguous determination of possible phase boundaries. We found less variability in the calculated self-diffusion constants however, which we used to determine the number of modes of FM that were diffusive.

### 2.2.3. Synthesis of In-Situ MOF Growth on Graphene Oxide Film

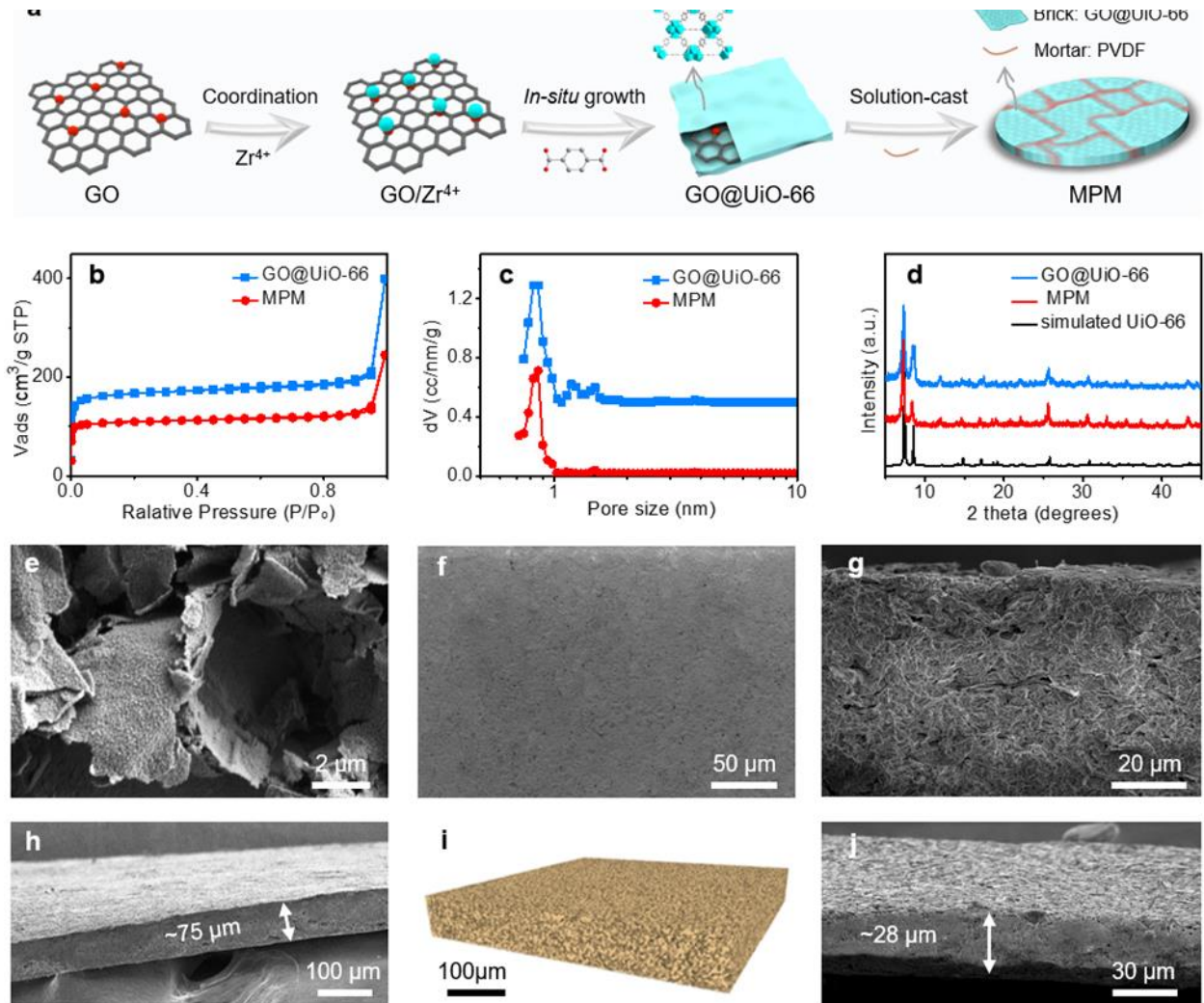


**Figure 7:** (a) Fabrication process of MPMs.  $N_2$  sorption isotherm curves (b) pore size distributions (c), XRD patterns (d) of simulated UiO-66, GO@UiO-66 and MPM. (e) SEM images of GO@UiO-66. Top (f) and cross-sectional (g, h, j) SEM views of two representative MPMs (i) Nano-CT reconstruction of MPM.

As demonstrated in previous reports, we developed a versatile process to make MPM with synthesized MOF powders and a polymer matrix. Unfortunately, such MOF powderglomerate membrane induces a significantly fluctuating ionic conductivity data. The fundamental problem can attribute to its intrinsic features of powder-based material, which tends to produce an unstable structure upon soaking in electrolyte.

#### 2.2.4. *Ionic conductivity measurement of MOF membrane*

To further investigate the electrochemical properties of cells employing the MPM with FM, the ionic conductivity was measured by a customized two-electrode conductivity cell (supplemental information). The LGE exhibited a superior conductivity at a wide temperature range. In contrast, the industry-standard liquid electrolyte (1 M LiPF<sub>6</sub> in ethylene carbonate/diethyl carbonate, EC/DEC, 1:1 in volume) suffered from rapid conductivity fading with decreasing temperature, suggesting the advantage of using LGE in extremely cold conditions. The MPM confined FM exhibited an ionic conductivity of ~0.14 mS/cm at -60°C. In contrast, a Celgard-based system showed less than 0.08 mS/cm at the same temperature and pressure (Fig. 8a, b). This dramatic difference is attributed to the continuous microporous channels formed in the MOF layers and strong affinity between FM and MOFs, which provides improved transport properties.

To probe the nano-confinement effect of the MPM at low temperatures beneath the vapor pressure of the FM electrolyte, a special testing system was designed to control and record the pressure inside the tested cells. The pressure of pure FM at different temperatures was collected, which was fitted with the theoretical data from the NIST database, indicating the viability of the testing system (Fig. 11). This setup was then applied to measure the ionic conductivity of the FM-soaked MPM at -40 °C under different pressures. By tuning the cell to 70 psi, 5 psi beneath the vapor pressure of the FM electrolyte, the cells utilizing MPM still offered an electrolyte conductivity of more than 0.02 mS/cm at -40 °C (Fig. 8c,d), indicating that the MPM retained a reasonable amount of FM inside their pores beneath the bulk vapor pressure, enabling Li<sup>+</sup> transport. On the contrary, the Celgard-based system produced an ionic

conductivity of less than 0.002 mS/cm due to inability of Celgard membranes to confine enough FM molecules at such pressure.

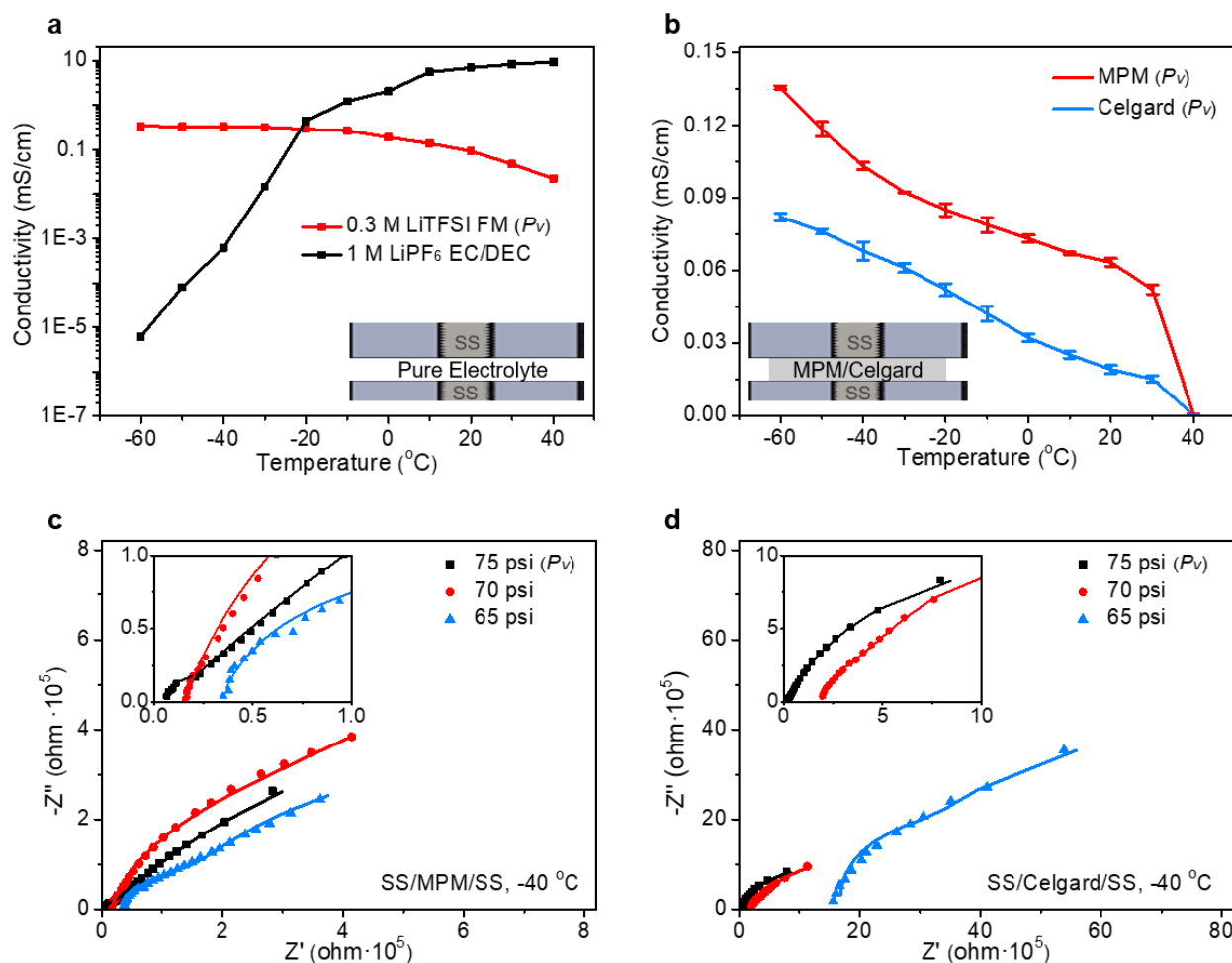


**Figure 8:** (a) Ionic conductivity of pure electrolyte. (b) Ionic conductivity of LGE with the presence of MPM or Celgard-based membranes as the separator at different temperatures. Nyquist impedance of cells with MPM (c) or Celgard-based (d) membrane as the separator at -40°C and different FM pressures.

### 2.2.5. Electrochemical performance comparison in flooded liquid and gas electrolyte

Given the confirmed structural stability, nano-confinement effects, and ionic conductivity results noted above, the MPM was considered as a promising porous membrane for reducing the pressure requirements for LGE. To further verify its application in a real battery system, the MPM was applied to Li-CF<sub>x</sub> primary cells. To ensure gas electrolyte transport, a composite cathode was fabricated by

introducing 20 wt.% of UiO-66 powders to blend  $\text{CF}_x$  with binder and conductive agent. The corresponding cells were assembled using  $\text{CF}_x$  composite cathode, Li metal as the anode, and the MPM or Celgard 2400 membranes as the separators. To evaluate the cell performance under reduced pressure, the same pressure control system noted before was used for operation. MPM-based cell produced an expected high capacity (940 mAh/g) at room temperature and vapor pressure, considerably higher than cells with Celgard 2400 membranes (906 mAh/g). At  $-40\text{ }^\circ\text{C}$  and vapor pressure, the cells with MPM provided an around 64 % room temperature capacity retention which was slightly higher than that of the Celgard membranes. In the same condition, the conventional liquid electrolyte system (1M  $\text{LiPF}_6$  EC/DEC) delivered nearly zero capacity at  $-40\text{ }^\circ\text{C}$  (Fig. 9a,b).

More interesting results were found during cell operation at reduced pressure (below  $P_v$ ). To ensure low-pressure gaseous phase operation, the cell pressure was *in-situ* monitored and maintained a nearly constant pressure of 70 psi during discharging operation (Fig. 9c). Notably, the cells with MPM can still maintain 52%, 42% and 23% of their room temperature capacity (at vapor pressure) at current density of 10, 20, and 40  $\text{mA g}^{-1}$ , respectively (Fig. 9d), in spite of the low conductivity of  $\text{CF}_x$  cathode and reduced charge-transfer kinetics at low temperature. In contrast, the cells with Celgard membrane under the same temperature and pressure produced negligible capacity ( $\sim 0.03\text{ mAh g}^{-1}$ ) at 10  $\text{mA g}^{-1}$ . Moreover, during discharging the voltage sharply decreased due to a large internal resistance (Fig.10), suggesting that the large pores of Celgard membrane were not able to retain gas electrolytes at reduced pressure, in agreement with the ionic conductivity measurements. The above results together highlight the advantage of MPMs toward confining LGE at reduced pressures for ultra-low temperature applications.

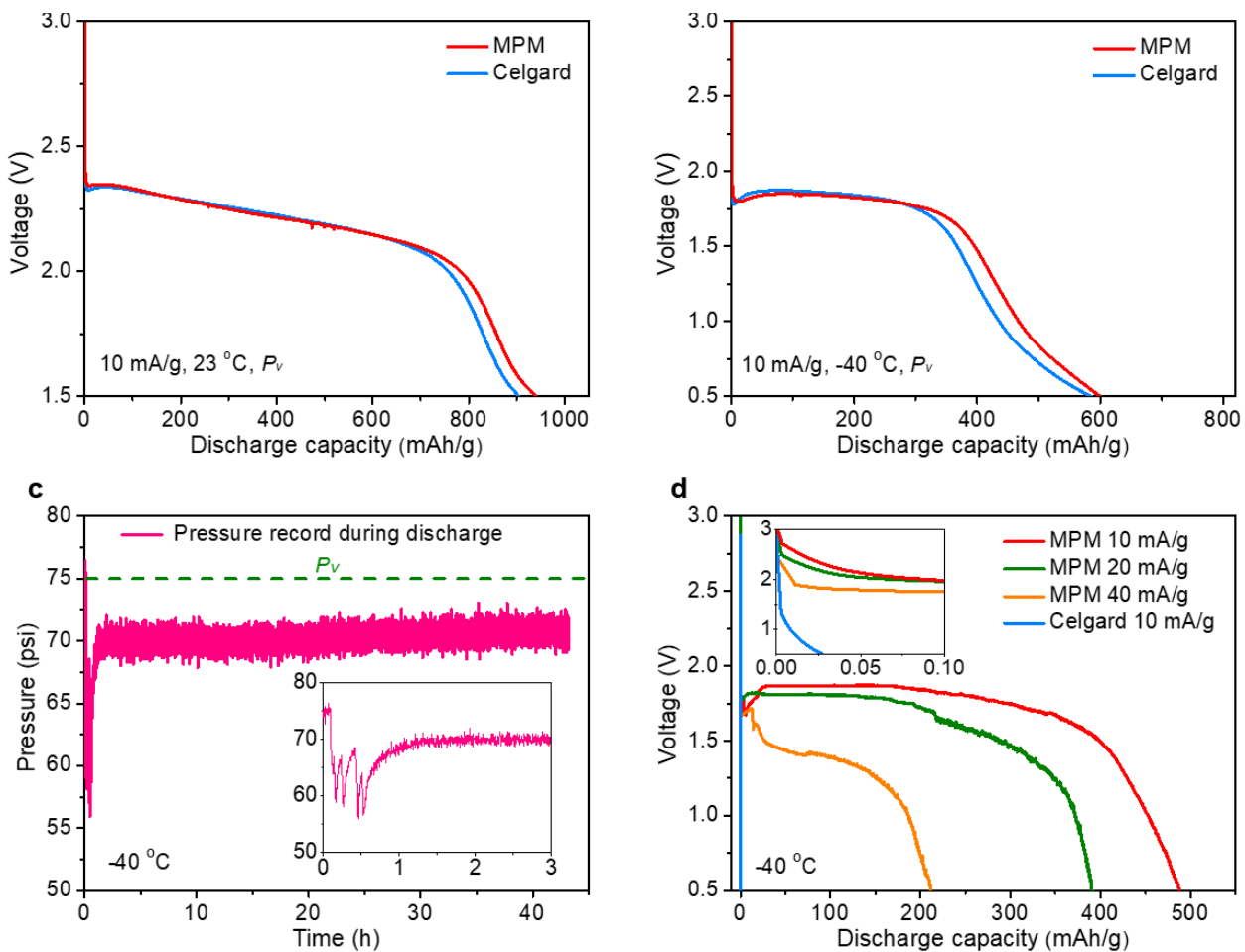


**Figure 9:** Graphic illustration of (A) Flooded liquefied FM system (D) Gaseous FM system. Discharge performance of Li/CFx cell using Celgard and MPM comparison at liquefied FM system(B) and gaseous FM system(E) at -40 °C (F) The FM pressure during the discharge process at gaseous FM system.

### 2.2.6. Investigation of interfacial impedance

To investigate the nano-confinement effect of the MPM at low temperatures beneath the vapor pressure of the FM electrolyte, the electrochemical impedance spectroscopy (EIS) was applied to a two-electrode cells. Lithium metal was placed as the anode and CF<sub>x</sub> mixed with 20%wt UiO-66 powders was considered as the cathodes, where Celgard and MPM was sandwiched between anode and cathode.

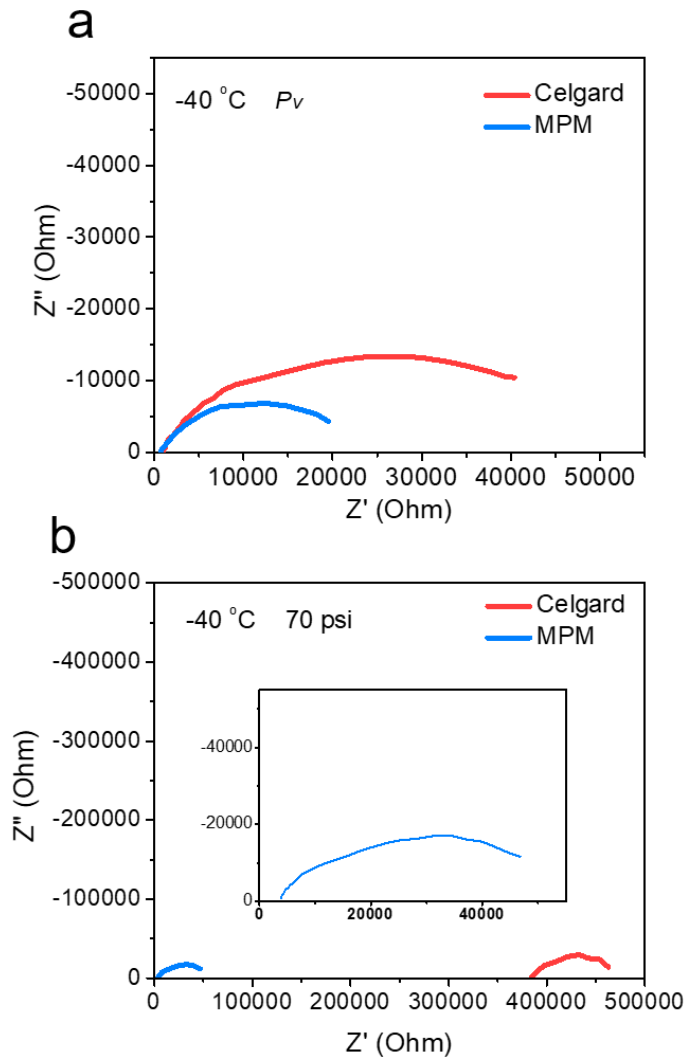


**Figure 10:** Nyquist impedance of Li/CF<sub>x</sub> mixed with 20% wt UiO-66 using Celgard and MPM at (a) vapor pressure and (b) 70 psi at  $-40\text{ }^{\circ}\text{C}$

From Fig 10 (a) and (b), it can be observed cell using MPM deliver lower charge transfer resistance at vapor pressure, whereas cell using Celgard experienced a significant increase of impedance when it was exposed to pressure beneath the vapor pressure. The above results proved the MPM's nano-confinement effect when pressure below vapor pressure.

Section 2.2 is coauthored with Guorui Cai, Dawei Xia, Amanda A. Chen, John Holoubek, Jonathan Scharf, Yangyuchen Yang, Ki Hwan Koh, Mingqian Li, Daniel M. Davies, Matthew Mayer, Tae Hee Han, Prof. Ying Shirley Meng, Prof. Tod A. Pascal and Prof. Zheng Chen. The thesis author is the primary author of this section.

### 3. Experimental Methods

Chemicals. N,N-Dimethylformamide (DMF), Fisher Scientific, 99.9%; ZrCl<sub>4</sub>, Alfa Aesar, > 99.5%; Cu(NO<sub>3</sub>)<sub>2</sub>·3H<sub>2</sub>O, Alfa Aesar, 99.0%; Terephthalic acid (BDC), Sigma-Aldrich, 98%; Biphenyl-1,4'-dicarboxylic acid (BPDC), Accela Chem Bio Inc., 97.0%; Benzene-1,3,5-tricarboxylic acid (BTC), Alfa Aesar, 98%; Benzoic acid, Sigma-Aldrich, > 99.5%; Polyvinylidene difluoride (PVDF), HSV-1800; Poly(vinylidene fluoride-co-hexafluoropropylene), PVDF-HFP 2801; N-Methyl-2-Pyrrolidone (NMP), Sigma-Aldrich, 99.5%; Acetic acid, glacial, Fisher Scientific, 99.7%; Hydrochloric acid (HCl), Fisher Scientific; Fluorinated graphite (CF<sub>x</sub>), ACS Materials; Lithium bis(trifluoromethane)sulfonimide (LiTFSI), BASF; Fluoromethane (FM), Air Liquide, 99.99%; Tetrahydrofuran (THF), Sigma-Aldrich, > 99.9%.

Synthesis. Preparation of GO@UiO-66. The graphene oxide (GO, 100 mg) prepared by a modified Hummers' method<sup>48</sup> were dispersed in 100 mL DMF by sonication. The DMF solutions (40 mL) of ZrCl<sub>4</sub> and BDC were added to the above GO dispersion in sequence. After adding 3 mL of acetic acid and stirring

at room temperature for 10 min, the mixture was allowed to be heated and stirred at 120 °C for 12 h in an oil bath. After cooling down to room temperature, the grey powder was collected via a centrifugation, and washed with DMF and methanol in sequence (each for 3 times). The obtained GO@UiO-66 was soaked with methanol overnight, and then was centrifuged and dried in vacuum under 120 °C for 1 day before any fabrication and characterization.

The preparation of metal-organic framework (MOF)-polymer membranes (MPMs). The resulted GO@UiO-66 and PVDF with a mass ratio of 4:1 was dispersed in NMP solution by a Thinky mixer. The obtained slurry was casted on one piece of glass substrate via a doctor blade to control their thickness. After drying in vacuum at 120 °C for 1 day, the membrane was elaborately peeled off from the glass and rolled by roller mill (Durst) to produce the final MPM. The MPM was heated at 120 °C in the glove box in vacuum overnight before electrochemical tests.

The preparation of UiO-66 for soaking tests and UiO-66-based MMMs. A solution comprised of ZrCl<sub>4</sub> (488 mg), BDC (344 mg), acetic acid (3.6 mL), and DMF (60 mL) were sealed in a Teflon reactor (100 mL) and then heated at 120 °C for 24 h. After cooling down to room temperature, the white powder was collected by a centrifugation, washed with DMF and methanol in sequence, and then dried in vacuum under 120 °C for 1 day before any fabrication and characterization.

Preparation of UiO-66 for mass change tests and porous additives of cathodes. A solution comprised of ZrCl<sub>4</sub> (875 mg), BDC (625 mg), acetic acid (50 mL), and DMF (250 mL) was prepared. The solution was then divided into four Teflon reactors (100 mL) and then heated at 120 °C for 24 h. After cooling down to room temperature, the white powder was collected by a centrifugation, washed with DMF and methanol in sequence, and then dried in vacuum under 120 °C for 1 day before any fabrication and characterization.

The preparation of HKUST-1. Typically, the BTC (1 g) and  $\text{Cu}(\text{NO}_3)_2 \cdot 3\text{H}_2\text{O}$  (2 g) were added into a mixture solution with DMF,  $\text{H}_2\text{O}$ , and ethanol (16 mL/16 mL/16 mL) and stirred for 15 min. The resulted blue mixture was then transferred into an oven and was allowed to react at 85 °C for 12 h. After cooling down to room temperature, the blue powder was collected by centrifugation, washed with DMF and methanol in sequence, and then dried in vacuum under 120 °C for 1 day before any fabrication and characterization.

The preparation of UiO-67 for soaking tests and UiO-67 based MMMs. The synthesis method of UiO-67 followed the procedure of UiO-66 (section 1.3) except for replacing BDC by BPDC in the same molar ratio.

The preparation of MOF-808. Typically, 0.583 g of  $\text{ZrCl}_4$  and 0.175 g of BTC was dissolved in 25 mL of DMF. Subsequently, 14 mL of acetic acid was added. After stirring for 5 min, the mixture was allowed to be heated at 135 °C for 24 h. The obtained powder was collected by centrifuged (washed with DMF for 3 times and then methanol for 3 times) and soaked in methanol for 1 day. Then the powder was dried in a vacuum oven under 120 °C for 1 day before any fabrication and characterization.

The preparation of MOF-based mixed matrix membranes (MMM). An acetone solution (8 mL) of MOF powders (0.3 g) and an NMP solution (0.7 mL) of PVDF-HFP (0.15 g) were prepared by sonication. The above solutions were mixed, vigorously shaken, and then under further sonication for 30 min. The mixture was transferred into a vacuum oven (~0.25 atm) for 40 min to remove the acetone solvent. Subsequently, the concentrated suspension was further homogenized by a Thinky mixer for 10 min. The resulted slurry was then poured onto a clean glass substrate, casted by a doctor blade to control the thickness (300-400  $\mu\text{m}$ ). The sample was dried at ambient pressure (60 °C) first and then at vacuum

(120 °C). The MMMs were easy to be peeled off from the substrate upon wetting with ethanol. The free-standing MMMs were heated at 120 °C in the glove box in vacuum overnight before electrochemical tests.

Fabrication of CFx (fluorinated graphite) cathodes. Typically, 240 mg of CFx was sufficiently mixed with 80 mg of UiO-66 and 40 mg of carbon black in the mortar by hand. The NMP solution containing 40 mg of PVDF were dropped into the above powder mixture. The homogeneous slurry obtained by a Thinky mixture was casted on clean Al foil. The electrode was dried in vacuum at 120 °C overnight before any use.

Electrochemical measurements. The ionic conductivity of the pure electrolyte of 0.3 M LiTFSI in FM and the selected electrolyte soaked Celgard membrane, MMM and MPM were measured by a customized two-electrode (Stainless Steel 316L) conductivity cell. The electrolyte composition was 0.3 M LiTFSI in FM with excessive LiTFSI and FM to ensure there was sufficient salt left after reaching the pressure below vapor pressure at the set temperature. It's noteworthy the 0.3 M LiTFSI in 1:4:95 vol% THF, CO<sub>2</sub>, FM was only used to measure the ionic conductivity of MMM for choosing the MOF candidates. The cell constant was frequently calibrated by using OAKTON standard conductivity solutions at 0.447, 1.5, 15 and 80 mS·cm<sup>-1</sup> respectively. A constant thickness spacer was positioned between the two electrodes which ensured no distance changes during multiple-time measurements. The electrolytic conductivity value was obtained with a floating AC signal at a frequency determined by the phase angle minima given by the electrochemical impedance spectroscopy (EIS) using the following equation:  $\sigma = K \cdot R^{-Q}$ , where R is the tested impedance( $\Omega$ ), K the cell constant(cm<sup>-1</sup>) and Q the fitting parameter.<sup>49</sup> All of data acquisition and output were done by LabView Software, which was also used to control an ESPEC BTX-475 programming temperature chamber to maintain the cell at a set temperature in 30 minutes intervals.

EIS measurements were conducted with a sinusoidal probe voltage of 5 mV from 1 mHz to 1 MHz in a customized high-pressure stainless-steel cell. The spectra were fitted by an equivalent circuit model using ZView software.

The pressure tuning process was finished by the customized tuning system, as shown in Figure 11. It consisted of one SPT25-10-1000A ProSense pressure transmitter with 0 to 1000 psi range, four Swagelok ball valves, one customized high-pressure cell, one Swagelok tube fitting and several PTFE thermal-resistant tubes. The pressure transmitter was connected to the customized cell through a T-sized Swagelok tube fitting of which the other side was connected to an Edwards vacuum pump using PTFE tubes. The pressure transmitter was opened during the whole experiment period to monitor the pressure change and the testing temperature was controlled by ESPEC BTX-475 programming temperature chamber to maintain the cell at a set temperature. All of the data transfer was controlled by the LabView program. During tuning process, the valve C and D was kept open and after the tuning process, valve C was close and valve D was kept open to record the pressure value during the discharge process. We decreased the pressure from vapor pressure to the pressure below vapor pressure at the set temperature controlled by valve B. When the pressure was stable at the set pressure at -40 °C, cells were tested by a Biologic SP-150 electrochemistry workstation.

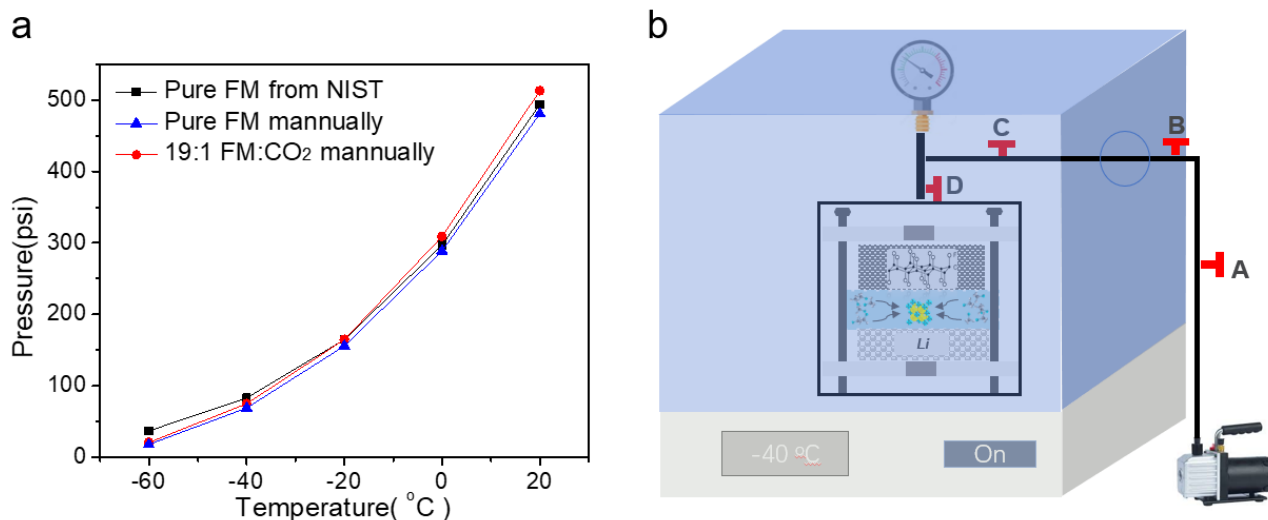


**Figure 11:** (a) Pressure calibration of vapor pressure of FM and the mixture of FM and CO<sub>2</sub> at different temperatures. (b) Schematic description of pressure tuning process.

Battery test under vapor pressure was performed by an Arbin battery test station (BT2043, Arbin Instruments, USA) and battery test under reduced pressure was performed by an Biologic SP-150 electrochemistry workstation in custom designed high-pressure stainless-steel coin cells, with Li metal (FMC Lithium, 1 mm thickness, 3/8 inch diameter) as the counter electrode and CFx (1/4 inch diameter) mixed with 20 % wt of UiO-66 as the working electrode. 5% CO<sub>2</sub> in FM was added to stabilize the lithium metal.<sup>12</sup> All of the electrochemical test and ionic conductivity test have included the CO<sub>2</sub> to keep consistent test system. Three layers of porous polypropylene separator (Celgard 2400, 25 μm) or one layer of MPM (~ 75 μm) was applied for all the electrochemical experiments.

**Material Characterizations.** Morphologies of various MOF powders and MOF membranes were detected by Scanning Electron Microscope (FEI XL30, UHR-SEM). Powder X-ray diffraction (XRD) patterns were measured on Bruker D2 Phaser (Germany) under Cu Kα radiation. N<sub>2</sub> adsorption/desorption isotherms were tested with Quantachrome instrument (QUADRASORB SI, American) at 77 K. The model for pore size distribution simulation was NLDFT. Degassing condition was set as 120 °C for 12 h. Fourier

transform-Infrared (FT-IR) spectra of different MOF powders were carried on Nicolet 6700 with Smart-iTR diamond ATR crystal using attenuated total reflectance mode. The spectrometer was equipped with a liquid nitrogen-cooled MCT-A detector to receive the IR signal from 600 to 4000  $\text{cm}^{-1}$ . Raman spectra of liquefied gas electrolytes were carried on Renishaw inVia confocal Raman microscope with an excitation wavelength of 532 nm calibrated with Si (520 nm) before test.

X-ray nano-computed tomography (Nano-CT) test was performed on the MPM sample, which was individually punched into a film with a radius of 2 mm and placed within a PTFE cylindrical tube with PTFE rod ends to provide sealing. The scan was conducted using a ZEISS Xradia 510 Versa micro-CT instrument with a voxel size of  $75\mu\text{m}$  and an exposure of 10 seconds. An X-ray energy of 80 keV with a current of  $87.6\ \mu\text{A}$  was used to collect 1801 projections with a high energy filter at a 4X magnification. The final reconstruction of the raw scan data was performed with a beam hardening constant of 0 and a center shift constant of -2.9 using software provided by ZEISS. Post measurement analysis was performed by Amira-Avizo using the Despeckle, Deblur, and Delineate modules for data sharpening and filtration provided by the software. The volume fraction and area of the MOF structure were determined with the Materials Analysis and Volume Fraction modules within Amira-Avizo.

Mass change test. Mass change test was done by soaking different MOF powders into a customized high-pressure stainless-steel cell filled with FM under different pressure for three days at room temperature. After the soaking process, most of FM was firstly purged out of the cell and then the cell was transferred into an Ar-filled glovebox to measure the total mass of soaked MOFs powders using a scientific scale with  $10^{-4}$  g accuracy. Subsequently, the MOF powders were rest and the mass was recorded. The normalized mass change is the mass of MOF powders after soaking process divided by the mass of UiO-

66 before soaking process. It's noticeable that there was less than 5% mass loss during sample transfer process.

The compatibility test of MOFs in FM. Stability tests for different MOF powders in FM were carried out at vapor pressure (500 psi) at room temperature for 3 days with excessive liquid FM immersing MOF particles. After the soaking process, BET, XRD, FT-IR and Raman analysis were done on the soaked MOF powders. As for the FT-IR and Raman, the exposed time of tested samples to the air was less than 30 seconds.

Stability tests for the MPMs and MMMs in selected electrolytes were carried out at vapor pressure (500 psi) at room temperature for 3 days with excessive 0.3 M LiTFSI in FM electrolytes. After the soaking process, the soaked samples were conducted the SEM analysis compared with the pristine films.

Computational details. The simulation parameters were described, where the FM properties were obtained via quantum mechanics (QM) calculations at the MP2/aug-cc-pVTZ level of theory using the Q-Chem 5.0 electronic structure package.<sup>50</sup> Initially, we optimized the UiO-66 starting structure using molecular dynamics (MD) simulations via the LAMMPS simulation engine.<sup>51</sup> The loading curves of FM in UiO-66 were then obtained from the optimized structure by Grand Canonical Monte-Carlo (GCMC) simulations using the MCCCSTowhee simulation package.<sup>52</sup> In each GCMC computation, 3 million moves were performed, and we tested that convergence was obtained in each simulation. The initial 2 million moves were used to stabilize the system, while the last 1 million moves were used to obtain the relevant statistics and absorption capacities.<sup>53,54</sup> After adsorbed FM capacities were determined, the system properties were further modeled and calculated via MD simulations. Details of MD simulations were mentioned as follows.

FM/UiO-66 and UiO-66 systems. For each MD simulation we started with the equilibrium geometry from 500 steps of conjugated gradient (CG) minimization (cell coordinates and atom positions) followed by 10 ps of canonical (constant particles, volume and temperature or NVT) dynamics to heat the system from 1 K to the defined temperature. Further, we ran iso-thermal iso-baric (constant particles, pressure, and temperature or NPT) dynamics for 1 ns followed by 0.8 ns NVT dynamics to equilibrate the system. The last 0.2 ps NVT data was used to collect thermodynamic statistics and to analyze the system properties. The temperature damping constant was 0.1 ps, and the pressure damping constant was 2.0 ps. The equations of motion used are those of Shinoda et al.,<sup>55</sup> which combine the hydrostatic equations of Martyna et al.<sup>56</sup> with the strain energy proposed by Parrinello and Rahman.<sup>57</sup> The time integration schemes closely follow the time-reversible measure preserving Verlet integrators derived by Tuckerman et al.<sup>58</sup>

Bulk FM systems. For bulk FM, a simulation cell comprising 216 molecules at the 298 K saturated vapor density 2.7688 mol/L from NIST database) was subjected to 500 steps of conjugated gradient (CG) minimization (cell coordinates and atom positions) followed by 10 ps of Langevin dynamics to heat the system from 1 K to a defined temperature. 1 ns NPT dynamics followed by 5.5 ns Langevin dynamics was applied to properly equilibrate the system. Longer simulation times, compared to FM/UiO-66 and UiO-66 systems, and the application of Langevin dynamic were to ensure thermal equipartition of the energy, due to the low density of a bulk FM system. This was followed by 0.7 ns of NVT dynamics, with statistics collected during the last 0.2 ps used to analyze the system properties. The temperature damping constant was 0.1 ps, and the pressure damping constant was 2.0 ps.

Self-diffusion constants and fluidicity factors. The self-diffusion constant  $D$  was obtained using the Green-Kubo VAC formulism in linear response theory:<sup>57</sup>

$$D = \frac{1}{N} \sum_1^N \int_0^\infty \langle v_i(t) \cdot v_i(0) \rangle dt$$

where  $t$  is time,  $v_i$  the axial COM velocity of molecule  $i$  and the brackets denote an autocorrelation that is summed over all molecules. These calculations were obtained from additional simulation in the canonical ensemble after pressure equilibration has been achieved. Snapshots of the system (atomic coordinates and velocities) were saved every 1 fs during a 0.5 ns simulation. Statistical averaging was performed in using 10 windows of 50 ps each. Our previous work has shown that trajectory windows of 50 ps were long enough to have converged self-diffusion constants by this approach.<sup>58</sup>

These self-diffusion constants were used to determine the fluidicity ( $f$ )-factor, the fraction of the  $3N$  translation modes corresponding to the fluid or diffusional parts of the dynamic system. Here, we compared the calculated self-diffusion constant of FM to the self-diffusion constant of a gas of hard sphere at the same density and temperature.<sup>59</sup>

## 4. Conclusion

In summary, the first part of Li/CFx batteries enabled by liquefied gas electrolyte showed the promising candidates for ultra-low temperature field. Further study will understand the distinct feature of LGE at low temperature field. The second part work shows strong confinement effects of gas molecules in sub-nanometer pores which leads to significantly increased mass uptake of molecules at pressure lower than the vapor pressure of the bulk counterpart. This was demonstrated by designing “brick-and-mortar”-like MPM membrane as an electrolyte host that consists of dense and continuous micropores from MOF building blocks. Both computational and experimental results showed that the electrolyte system based on

liquefied FM molecules via capillary condensation in MOFs lowers the equilibrium vapor pressure of FM. The resulted MPM with FM exhibited high structural integrity, decent ion conductivity, and high FM retention, which enabled the operation of high-energy Li cells at extremely low temperatures and reduced working pressure. The unique properties endowed by molecule confinement in nanopores can be extended to design other types of ionic conductive structures for different electrochemical systems, thus opening up new opportunities for emerging applications without sacrificing ease of manufacturability and operation.

## Reference

- [1] Winter, M.; Barnett, B.; Xu, K. Before Li Ion Batteries. *Chem. Rev.* **2018**, *118* (23), 11433–11456.
- [2] Goodenough, J. B.; Kim, Y. Challenges for Rechargeable Li Batteries. *Chem. Mater.* **2010**, *22* (3), 587–603.
- [3] Dong, X.; Guo, Z.; Guo, Z.; Wang, Y.; Xia, Y. Organic Batteries Operated at  $-70^{\circ}\text{C}$ . *Joule* **2018**, *2* (5), 902–913.
- [4] Dong, X.; Lin, Y.; Li, P.; Ma, Y.; Huang, J.; Bin, D.; Wang, Y.; Qi, Y.; Xia, Y. High-Energy Rechargeable Metallic Lithium Battery at  $-70^{\circ}\text{C}$  Enabled by a Cosolvent Electrolyte. *Angewandte Chemie International Edition* **2019**, *58* (17), 5623–5627.
- [5] Smart, M. C.; Ratnakumar, B. V.; Ewell, R. C.; Surampudi, S.; Puglia, F. J.; Gitzendanner, R. The Use of Lithium-Ion Batteries for JPL's Mars Missions. *Electrochimica Acta* **2018**, *268*, 27–40.
- [6] Chin, K. B.; Brandon, E. J.; Bugga, R. V.; Smart, M. C.; Jones, S. C.; Krause, F. C.; West, W. C.; Bolotin, G. G. Energy Storage Technologies for Small Satellite Applications. *Proceedings of the IEEE* **2018**, *106* (3), 419–428.
- [7] Jaguemont, J.; Boulon, L.; Dubé, Y. A Comprehensive Review of Lithium-Ion Batteries Used in Hybrid and Electric Vehicles at Cold Temperatures. *Applied Energy* **2016**, *164*, 99–114.
- [8] Zhang, S. S.; Xu, K.; Jow, T. R. The Low Temperature Performance of Li-Ion Batteries. *Journal of Power Sources* **2003**, *115* (1), 137–140.
- [9] Huang, C.-K.; Sakamoto, J. S.; Wolfenstine, J.; Surampudi, S. The Limits of Low-Temperature Performance of Li-Ion Cells. *J. Electrochem. Soc.* **2000**, *147* (8), 2893–2896.
- [10] Zhu, G.; Wen, K.; Lv, W.; Zhou, X.; Liang, Y.; Yang, F.; Chen, Z.; Zou, M.; Li, J.; Zhang, Y. Materials Insights into Low-Temperature Performances of Lithium-Ion Batteries. *Journal of Power Sources* **2015**, *300*, 29–40.
- [11] Zhang, S. S.; Xu, K.; Jow, T. R. Low Temperature Performance of Graphite Electrode in Li-Ion Cells. *Electrochimica Acta* **2002**, *48* (3), 241–246.
- [12] Li, Q.; Lu, D.; Zheng, J.; Jiao, S.; Luo, L.; Wang, C.-M.; Xu, K.; Zhang, J.-G.; Xu, W. Li<sup>+</sup>-Desolvation Dictating Lithium-Ion Battery's Low-Temperature Performances. *ACS Appl. Mater. Interfaces* **2017**, *9* (49), 42761–42768.
- [13] Charlaix, E.; Ciccotti, M. Capillary Condensation in Confined Media. *Handbook of Nanophysics*, CRC Press **June 2010**, vol. 1
- [14] Barsotti, E.; Tan, S. P.; Saraji, S.; Piri, M.; Chen, J. H. A Review on Capillary Condensation in Nanoporous Media: Implications for Hydrocarbon Recovery from Tight Reservoirs. *Fuel* **2016**, *184*, 344–361
- [15] Rustomji, C. S.; Yang, Y.; Kim, T. K.; Mac, J.; Kim, Y. J.; Caldwell, E.; Chung, H.; Meng, Y. S. Liquefied Gas Electrolytes for Electrochemical Energy Storage Devices. *Science* **2017**, eaal4263

- [16] Kandiah, M., M. H. Nilsen, S. Usseglio, S. Jakobsen, U. Olsbye, M. Tilset, C. Larabi, E. A. Quadrelli, F. Bonino and K. P. Lillerud. "Synthesis and Stability of Tagged UiO-66 Zr-MOFs." *Chemistry of Materials* **2010** 22(24): 6632-6640
- [17] Katz, Michael J., Zachary J. Brown, Yamil J. Colón, Paul W. Siu, Karl A. Scheidt, Randall Q. Snurr, Joseph T. Hupp, and Omar K. Farha. 'A facile synthesis of UiO-66, UiO-67 and their derivatives', *Chemical Communications*, **2013** 49: 9449-51.
- [18] Yang Y.; Davies D. M.; Yin Y.; Borodin O.; Lee J. Z.; Fang C.; Olguin M.; Zhang Y.; Sablina E. S.; Wang X.; Rustomji C. S. High-efficiency lithium-metal anode enabled by liquefied gas electrolytes. *Joule* 2019, 3, 1986-2000
- [19] Bai, S., Liu, X., Zhu, K., Wu, S., & Zhou, H. (2016). Metal–organic framework-based separator for lithium–sulfur batteries. *Nature Energy*, 1(7), 1-6.
- [20] Smart, M. C., Ratnakumar, B. V., Ewell, R. C., Surampudi, S., Puglia, F. J., & Gitzendanner, R. (2018). The use of lithium-ion batteries for JPL's Mars missions. *Electrochimica Acta*, 268, 27-40.
- [21] Chin, K. B., Brandon, E. J., Bugga, R. V., Smart, M. C., Jones, S. C., Krause, F. C., William C. W. & Bolotin, G. G. (2018). Energy storage technologies for small satellite applications. *Proceedings of the IEEE*, 106(3), 419-428.
- [22] Rodrigues, M. T. F., Babu, G., Gullapalli, H., Kalaga, K., Sayed, F. N., Kato, K., Jarin J. & Ajayan, P. M. (2017). A materials perspective on Li-ion batteries at extreme temperatures. *nature energy*, 2(8), 1-14.
- [23] Jaguemont, J., Boulon, L. & Dubé, Y. A comprehensive review of lithium-ion batteries used in hybrid and electric vehicles at cold temperatures. *Appl. Energy* 164, 99-114 (2016).
- [24] Gupta, A. & Manthiram, A. Designing advanced lithium-based batteries for low-temperature Conditions. *Adv. Energy Mater.* 2001972 (2020).
- [25] Fan, X.; Ji, X.; Chen, L.; Chen, J.; Deng, T.; Han, F.; Yue, J.; Piao, N.; Wang, R.; Zhou, X.; Xiao, X. All-temperature batteries enabled by fluorinated electrolytes with non-polar solvents. *Nat. Energy* 2019, 4, 882-890
- [26] Cai, G., Holoubek, J., Xia, D., Li, M., Yin, Y., Xing, X., Ping, L. & Chen, Z. (2020). An ester electrolyte for lithium–sulfur batteries capable of ultra-low temperature cycling. *Chemical Communications*, 56(64), 9114-9117.
- [27] Li, Q.; Lu, D.; Zheng, J.; Jiao, S.; Luo, L.; Wang, C. M.; Xu, K.; Zhang, J. G.; Xu, W. Li+-desolvation dictating lithium-ion battery's low-temperature performances. *ACS Appl. Mater. Interfaces* 2017, 9, 42761-42768.
- [28] Ji, Y.; Wang, C. Y. Heating strategies for Li-ion batteries operated from subzero temperatures. *Electrochim. Acta* 2013, 107, 664-674.
- [29] Wang, C.-Y.; Zhang, G.; Ge, S.; Xu, T.; Ji, Y.; Yang, X.-G.; Leng, Y. Lithium-ion battery structure that self-heats at low temperatures. *Nature* 2016, 529, 515-518.
- [30] Rustomji, C. S.; Yang, Y.; Kim, T. K.; Mac, J.; Kim, Y. J.; Caldwell, E.; Chung, H.; Meng, Y. S. Liquefied gas electrolytes for electrochemical energy storage devices. *Science* 2017, 356, 6345.

- [31] Yang Y.; Davies D. M.; Yin Y.; Borodin O.; Lee J. Z.; Fang C.; Olguin M.; Zhang Y.; Sablina E. S.; Wang X.; Rustomji C. S. High-efficiency lithium-metal anode enabled by liquefied gas electrolytes. *Joule* 2019, 3, 1986-2000.
- [32] Yang, Y.; Yin, Y.; Davies, D. M.; Zhang, M.; Mayer, M.; Zhang, Y.; Sablina, E. S.; Wang, S.; Lee, J. Z.; Borodin, O. A.; Rustomji, C. S.; Liquefied gas electrolytes for wide-temperature lithium metal batteries. *Energy Environ. Sci.* 2020, 13, 2209-2219
- [33] Fisher, L. R. & Israelachvili, J. N. Direct experimental verification of the Kelvin equation for capillary condensation. *Nature* 277, 548-549 (1979).
- [34] Mitropoulos, A. The Kelvin equation. *J. Colloid Interface Sci.* 317, 643-648 (2008).
- [35] Li, L. & Sheng, J. J. Nanopore confinement effects on phase behavior and capillary pressure in a Wolfcamp shale reservoir. *J. Taiwan Institute Chem. Engineers* 78, 317-328 (2017).
- [36] Barsotti, E., Tan, S. P., Saraji, S., Piri, M. & Chen, J. H. A review on capillary condensation in nanoporous media: implications for hydrocarbon recovery from tight reservoirs. *Fuel* 184, 344-361 (2016).
- [37] Horikawa, T., Do, D. D. & Nicholson, D. Capillary condensation of adsorbates in porous materials. *Adv. Colloid Interface Sci.* 169, 40-58 (2011).
- [38] Aukett, P. N., Quirke, N., Riddiford, S. & Tennison, S. R. Methane adsorption on microporous carbons-a comparison of experiment, theory, and simulation. *Carbon* 30, 913-924 (1992).
- [39] Li, B., Wen, H. M., Zhou, W., Xu, J. Q. & Chen, B. Porous metal-organic frameworks: promising materials for methane storage. *Chem* 1, 557-580 (2016).
- [40] Furukawa, H., Cordova, K. E., O'Keeffe, M. & Yaghi, O. M. The chemistry and applications of metal-organic frameworks. *Science* 341, 1230444 (2013).
- [41] Zhou, H.-C. & Kitagawa, S. Metal-organic frameworks (MOFs). *Chem. Soc. Rev.* 43, 5415-5418 (2014).
- [42] Cai, G., Ding, M., Wu, Q. & Jiang, H.-L. Encapsulating soluble active species into hollow crystalline porous capsules beyond integration of homogeneous and heterogeneous catalysis. *Natl. Sci. Rev.* 7, 37-45 (2020).
- [43] Peng, Y., Li, Y., Ban, Y., Jin, H., Jiao, W., Liu, X., & Yang, W. (2014). Metal-organic framework nanosheets as building blocks for molecular sieving membranes. *Science*, 346(6215), 1356-1359.
- [44] Chen, Z., Li, P., Anderson, R., Wang, X., Zhang, X., Robison, L., Redfern, L.R., Moribe, S., Islamoglu, T., Gómez-Gualdrón D.A., Yildirim T., Stoddart J.F., & Farha, O.K. (2020). Balancing volumetric and gravimetric uptake in highly porous materials for clean energy. *Science*, 368(6488), 297-303.
- [45] Li, S., Dong, Y., Zhou, J., Liu, Y., Wang, J., Gao, X., Han Y., Qi, P. & Wang, B. (2018). Carbon dioxide in the cage: manganese metal-organic frameworks for high performance CO<sub>2</sub> electrodes in Li-CO<sub>2</sub> batteries. *Energy & Environmental Science*, 11(5), 1318-1325.
- [46] Chiochan, P., Yu, X., Sawangphruk, M. & Manthiram, A. A metal organic framework derived solid electrolyte for lithium-sulfur batteries. *Adv. Energy Mater.* 10, 2001285, (2020).

- [47] Park, S., Lee, K. S., Bozoklu, G., Cai, W., Nguyen, S. T., & Ruoff, R. S. (2008). Graphene oxide papers modified by divalent ions—enhancing mechanical properties via chemical cross-linking. *ACS nano*, 2(3), 572-578.
- [48] Rustomji, C. S., Mac, J., Choi, C., Kim, T. K., Choi, D., Meng, Y. S., & Jin, S. (2016). Thin-film electrochemical sensor electrode for rapid evaluation of electrolytic conductivity, cyclic voltammetry, and temperature measurements. *Journal of Applied Electrochemistry*, 46(1), 59-67.
- [49] Plimpton, S. Fast parallel algorithms for short-range molecular dynamics, *J. Comp. Phys.* 117, 1-19 (1995).
- [50] Martin, M. G. MCCCSTowhee: a tool for Monte Carlo molecular simulation, *Mol. Simulat.* 39, 1212-1222 (2013).
- [51] Cmarik, G. E., Kim, M., Cohen, S. M. & Walton, K. S. Tuning the adsorption properties of UiO-66 via ligand functionalization. *Langmuir* 28, 15606-15613 (2012).
- [52] Cavka, J. H., Grande, C. A., Mondino, G. & Blom, R. High pressure adsorption of CO<sub>2</sub> and CH<sub>4</sub> on Zr-MOFs. *Ind. Eng. Chem. Res.* 53, 15500-15507 (2014).
- [53] Shinoda, W., Shiga, M. & Mikami, M. Rapid estimation of elastic constants by molecular dynamics simulation under constant stress. *Phys. Rev. B* 69, 134103 (2004).
- [54] Martyna, G. J., Tobias, D. J. & Klein, M. L. Constant pressure molecular dynamics algorithms. *J. Chem Phys.* 101, 4177-4189 (1994).
- [55] Parrinello, M. & Rahman, A. Polymorphic transitions in single crystals: a new molecular dynamics method. *J. Appl. Phy.* 52, 7182-7190 (1981).
- [56] Tuckerman, M. E., Alejandre, J., López-Rendón, R., Jochim, A. L. & Martyna, G. J. A Liouville-operator derived measure-preserving integrator for molecular dynamics simulations in the isothermal-isobaric ensemble. *J. Phys. A* 39, 5629-5651 (2006).
- [57] Tildesley, D. J. & Allen, M. P. *Computer simulation of liquids.* (Oxford Univ. Press, Oxford [England]; New York, 1987).
- [58] Pascal, T. A., Lin, S. T. & Goddard III, W. A. Thermodynamics of liquids: standard molar entropies and heat capacities of common solvents from 2PT molecular dynamics. *Phys. Chem. Chem. Phys.* 13, 169-181 (2011).
- [59] McQuarrie, D. A. *Statistical Mechanics,* (Harper & Row: New York, 1976)